UiT
THE ARCTIC
UNIVERSITY
OF NORWAY

Department of Physics and Technology

# Short-term wind power prediction based on Markov chain and numerical weather prediction models: A case study of Fakken wind farm

—

**Morten Jacobsen**
*EOM-3901 Master’s Thesis in Energy, Climate and Environment*

*June 2014*

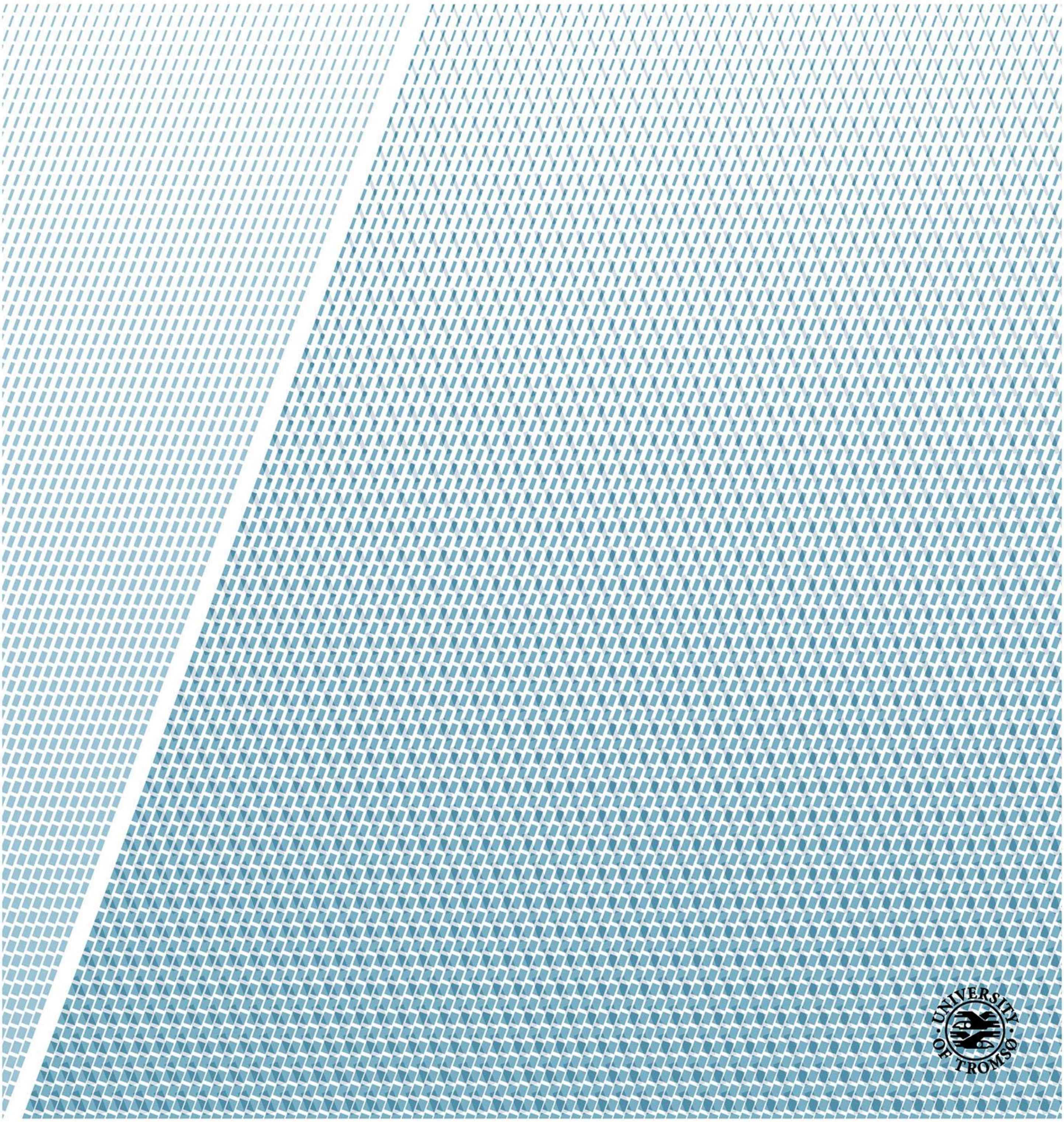

If you do tomorrow what you did today, you will get tomorrow what you got today.

— *Benjamin Franklin*

# Abstract

Rising energy demands and a growing focus on sustainable development have made electricity production from wind energy an attractive alternative to fossil fuels. However the natural variability of wind makes it challenging to implement wind energy into the electrical grid. Accurate and reliable wind power predictions are seen as a key element for an increased penetration of wind energy.

This study presents a set of statistical power prediction models using the concept of Markov chains, based on various input parameters, such as wind speed, direction and power output. The models have been trained and tested using numerical weather predictions and historical data obtained from a meteorological station and wind turbine at Fakken wind farm in the time period 2. May 2013 - 31. March 2014. Several of the models were found to have lower NRMSE than the currently used persistent model (19.08 %), with the best performing model having a NRMSE of 16.84 %. This 2.25 % lower NRMSE corresponds to approximately $3.1 \cdot 10^6$ kWh of the anually electricity production from Fakken wind farm.

A statistical analysis of Fakken wind farm showed the majority of winds occurring from the straits between Arnøya and Lenangsøyra to the southeast and between Reinøya and Lenangsøyra to the south. Winds were also commonly seen from southwest and to the northwest, while eastern and northeastern winds were rarely observed. Westerly winds were found to be much more tubulent than other directions, with a generally lower power output observed. This is most likely due to the occurerence of mountain waves for winds crossing the mountain range to the west.

# Acknowledgements

First of all I would like to thank my supervisor Yngve Birkelund for all the time you have dedicated to help me with this thesis. The results would not have been the same without your guidance and ideas. Not least for suggesting this thesis in the first place when things didn't quite work out as expected with Dyrøy.

I would also like to thank Svein Erik Thyrhaug and Ronald Hardersen at Troms Kraft for letting me use data from Fakken wind farm in my thesis and for our meetings where you provided me with valuable information and feedback. I am very grateful for the time you have invested in me and this thesis.

A special thanks to Eirik Mikal Samuelsen at MET, for providing me with the NWP data, teaching me about meteorology and answering my questions. I appreciate your friendliness and willingness to help me, even when you were busy.

To my beloved Maria, always being there for me, supporting me and sticking up with my many late hours. I love you very much.

To all the awesome people at Norutbrakka and especially Team Double Bounce Scattering. This has been 5 incredible years I will never forget.

Last but not least, a big thanks to the universe for skipping spring in Tromsø this semester and delaying the summer by several weeks. Nice and sunny weather would have made this journey unbearable.

*Morten Jacobsen*
*Tromsø, June 2014*

# Contents

# Abbreviations

| | |
|---|---|
| ABL | Atmospheric boundary layer |
| HAWT | Horizontal axis wind turbine |
| MC | Markov chain |
| NRMSE | Normalized root mean square error |
| NWP | Numerical weather prediction |
| PM | Persistent model |
| RMSE | Root mean square error |
| rpm | Rotations per minute |
| STD | Standard deviation |

# List of Figures

# List of Tables

# Chapter 1

# Introduction

## 1.1 Short-term wind power prediction

According to the latest IPCC-report the dominant cause of the global warming occurring since the mid-20th century is extremely likely to be due to anthropogenic influence [IPCC, 2014]. Nevertheless the worlds total energy consumption continues to increase annually, as does the demand for future energy production, and fossil fuels are by far the most dominant energy sources used today [BP, 2013]. In order to face the challenging climate change and at the same time meet the energy needs of tomorrow, reliable and sustainable alternatives to fossil fuels most be found and developed.

Harvesting the energy from renewable energy sources is considered to be one of the leading solutions to this challenge [EREC, 2005]. Wind is one such source with a great future potential. Looking at for instance the theoretical potential of wind energy on the earth, it has been determined to be in the range of $110 \cdot 10^{12} \pm 50 \cdot 10^{12}$ GJ/yr [Rogner et al.]. Taking into account the technical limitations of the current technology this number is reduced to $1500 \cdot 10^9 - 5700 \cdot 10^9$ GJ/yr and taking into account also the practical limitations such as conflicting land uses and remoteness the potential is estimated to be about $250 \cdot 10^9 - 1200 \cdot 10^9$ GJ/yr [Rogner et al.], or in a more commonly known energy measure $4.2 \cdot 10^9$ - $200 \cdot 10^9$ GWh/yr. This is approximately 34 000 to 162 000 times the electricity produced in Norway in 2010 (123 630 GWh/yr) [SSB, 2014].

However, there are some challenges connected with harvesting the wind energy which must be dealt with. One of the greatest is the natural variability of the wind. The global weather system is both complex and dynamic, making it hard to accurately predict the future wind parameters such as speed and direction, and great variations may occur over short time scales [Marquis et al., 2011].

The electricity generation in a region usually consists of a mix between three types of power plants: slow-start power plants, such as coal and nuclear plants, fast-start power plants, such as natural gas and hydroelectric plant, and variable renewable energy sources such as wind farms and solar power. At all times these generation units must be controlled by a balancing authority to ensure both a stable electricity supply corresponding to the consumer demand and to maintain a mixture of electricity generation which will give the lowest cost possible for the consumers [Yoder et al., 2013].

Being a variable energy resource, wind energy must be used as it is produced. A higher penetration of wind energy in the grid would therefore mean a higher degree of uncertainty. This makes it difficult for the balancing authority to plan how to meet the energy demand, as slow-start power plants will not be able to react rapidly to changes in the power load and they will not run as efficiently at lower capacity, while fast-start power plants can respond more quickly to the changes in demand, but at the cost of usually being more expensive [Yoder et al., 2013]. A higher degree of uncertainty in the grid would require more flexibility in the system, such as for instance keeping more reserves on-line as a backup, which again would lead to higher operating costs. As noted by Pourmousavi Kani and Ardehali [2011], very short-term variations (seconds and minutes) in wind power may also cause voltage and frequency fluctuations, especially in the event of cut-off speed.

Wind energy also causes some economically challenges for the power production companies, as they have to make estimates of how much power they have available for sale. Wrong estimates of the power production would lead to the companies having to buy expensive last minute power to cover the guaranteed power delivery for underproduction, or having to sell the power cheap in the case of overproduction.

Accurate wind power predictions is therefore a key element for an increased penetration of wind energy. This would not only make it easier to implement wind energy into the grid, it would also reduce the operational cost and make it easier for the power production companies to make more accurate predictions of how much energy they can sell on the marked.

## 1.2 Former research

The stochastic nature of wind makes it difficult to develop models which accurately predicts future wind speed and direction, thus also the future power output from a wind turbine. As a result, many different approaches have been tried to find the ideal power prediction model. This is especially seen in the work by Giebel et al. [2011] which gives an extensive literature overview of the state of the art short-term wind power prediction models, based on review of more than 380 journal and conference papers.

Wang et al. [2011] divides the prediction horizon into the following categories:

1. Immediate-short-term: From seconds up to 8 hours ahead forecasts,

| Time scale | Range | Application |
|---|---|---|
| Immediate-short-term | 8-hours ahead | - Real-time grid operations<br>- Regulation actions |
| Short-term | Day ahead | - Economic load dispatch planning<br>- Load reasonable decisions<br>- Operational security in electricity marked |
| Long-term | Multiple days ahead | - Maintenance planning<br>- Operation management<br>- Optimal operating cost |

Table 1.1: Time scale of forecast models and their applications [Wang et al., 2011].

2. Short-term: A day ahead forecasts,
3. Long-term: Multiple days ahead forecasts,

with the applications for each time horizon given in Table 1.1.

There are mainly two approaches used to when developing wind power prediction models: (i) a physical approach and (ii) a statistical approach [Giebel et al., 2011].

The former is a deterministic method which use physical considerations and input data to make predictions of the future power output [Carpinone et al., 2010]. These physical models are based on predictions of the lower atmosphere or numerical weather predictions (NWP) using input data such as temperature, pressure, surface roughness and obstacles obtained from weather forecasts [Wang et al., 2011].

The statistical approach predicts the future power output using historical obtained data, which could also include NWP results, and is a pure mathematical approach which does not consider any of the physical processes of wind [Carpinone et al., 2010]. The main idea is use these vast amounts of historical data to find a relationship to the power output. This typically involve time series analysis [Wang et al., 2011] and artificial neural networks, which often include the use of recursive techniques . For look-ahead times above 3-6 hours, models using a time series approach are usually outperformed by models involving a NWP [Giebel et al., 2011].

In order to get the best from each approach, a hybrid approach is typically used in most operational and commercial models today [Giebel et al., 2011]. Table 1.2 shows an overview of some of the wind forecasting models described by Wang et al. [2011], with their corresponding time horizon and approach.

| Model | Time horizon | Approach |
|---|---|---|
| WPMS | Immediate-short-term | Statistical |
| ANEMOS | Immediate-short-term, short-term | Statistical & Physical |
| ARMINES (A WPPS) | Immediate-short-term, short-term | Statistical & Physical |
| WPPT | Short-term | Statistical |
| Prediktor | Short-term | Physical |
| Previento | Long-term | Statistical & Physical |
| WEPROG | Long-term | Statistical & Physical |

Table 1.2: Some forecasting models for wind speed and power with their respective time horizon and approach used [Wang et al., 2011].

Forecast models used to predict more specific events or scenarios of power production are also being developed. In a recent study Bossavy et al. [2013] notes the lack of ability of current forecasting models to properly handle extreme situations related to wind generation, being a result of either extreme weather phenomena or critical periods for power system operation. A ramp is one such event, defined in the study as a steep and high increase or drop in power production from a wind farm within a time period of a few hours. The study proposes a methodology, which used together with numerical weather prediction ensembles, provides reliable forecasts with greater accuracy regarding climatology

Due to its simplicity and because many natural processes are considered as Markov processes [Shamshad et al., 2005], Markov chains have become a popular tool for developing wind power prediction models based on time series analysis. A Markov chain represents a system which, based on the input data, calculates the probability of going from one state to another. The order of the Markov chain decides how many previous time steps influencing the probability distribution of the current state. Such states could for instance represent a given power output, wind direction or wind speed. Another advantage using Markov chain is the possibility of not only making point predictions, but also probabilistic forecasts, , i. e. give information about how likely it is for a given prediction to occur.

A study by Shamshad et al. [2005] discuss how first and second order Markov chain models can be used for generating synthetic wind speed time series, which may further be used as input to a wind energy system. Carpinone et al. [2010] recommends instead to use wind power measurements directly as input to a Markov chain model in making a immediate-term forecast of the power . Argument being that for wind speed forecasts, the forecast would have to model the wind farm power curve of interest, take into account individual turbine curves, site orographic characteristics and wake effects, before finally converting the wind speed forecast into a power forecast. A process which could amplify the prediction error and which would be avoided using power data directly.

Instead of giving a specific wind speed forecast or power forecast Yoder et al. [2013] suggest using Markov chain models for predicting the 1 hour ahead categorical change in the wind power. In this case the power change in the last hour, the current wind power and the 20-minute power trend are used to provide a probabilistic forecast of three states, -1: a negative trend, 0: no change is expected and 1: a positive trend is predicted.

## 1.3 Purpose of the study

Fakken wind farm on Vannøya in Troms county was completed in the end of 2012 and consist of 18 Vestas V90 3.0MW horizontal axis wind turbines (HAWT). Annually the farm is expected to produce 138 GWh, enough power to supply about 7000 households [Troms Kraft AS, 2012].

The main purpose of this study is to use wind and power data recorded from a reference turbine and a meteorological station at Fakken wind farm to develop a power prediction model with a 2-hour prediction horizon (defined in this study as a short-term prediction), using the concept of Markov chains. The model will be tested using various input parameters, such as the measured power and wind data and forecast wind speed and direction obtained using numerical weather predictions (NWP).

It is expected that winds blowing from the west are more turbulent than other directions due to a local mountain range causing a weather phenomena known as mountain waves. It has also been suggested that the mountain range between Norway and Sweden to the southeast, causing regional mountain waves, may also influence the power production on Fakken wind farm. An analysis of the statistical properties of measured power and wind data will therefore also be given and related to the topography and surroundings of the wind farm site.

## 1.4 Structure of the study

This study is divided into 6 chapters. First chapter provided the motivation and purpose of this study. Wind theory and statistical theory are given in chapter 2, while information of the site and data collection are given in chapter 3. This is also where the prediction models are described. Results are shown in chapter 4 and discussed in chapter 5. In chapter 6 the study is concluded together with suggestions for further research.

# Chapter 2

# Theory

## 2.1 Source of wind energy

Wind energy, or simply wind, is the kinetic energy of air in motion. As stated by [Andrews and Jelley, 2007], the main source for wind energy is solar radiation. Radiation incident on the earth from the sun will mainly be absorbed by the earths surface, heating it, while the rest of the radiation will either heat up the atmosphere or be reflected by clouds, aerosols and gases in the atmosphere [Houghton, 2009]. Due to the shape of the earth, incident radiation hits the earth at different angles. At equatorial latitudes the incoming radiation will be close to perpendicular to the surface, while at higher latitudes, the same amount of radiation will be spread over a much greater surface area. As a result, the earth will in general receive a lot more energy at lower latitudes than higher latitudes, which results in a unbalance in the energy system. In addition to this effect, the heat capacity of the various materials differ from each other, thus the energy absorbed by the surface itself will also vary. This leads to temperature variations, which again leads to pressure gradients and in order to balance the system gas molecules in the air will start to move, causing convection.

Figure 2.1 shows an illustration of a simple convection cell. As air is heated up, it becomes less dense and the pressure decreases, creating a low pressure as can be seen to the right hand side in the figure. The heated air will start to rise in the atmosphere due to being less dense than nearby air parcels, but as it rises higher up in the atmosphere it will start to cool down again. In addition, the gravitational force acting on the air parcels decreases with height, i. e. air parcels with same temperature at two different heights will have different pressure forces acting on them. This causes pressure gradients, and high pressured air molecules next to the low pressure will start to move towards the low pressure. Simultaneously the air molecules from the low pressure will now start moving towards the illustrated high pressure as it is cooled down.

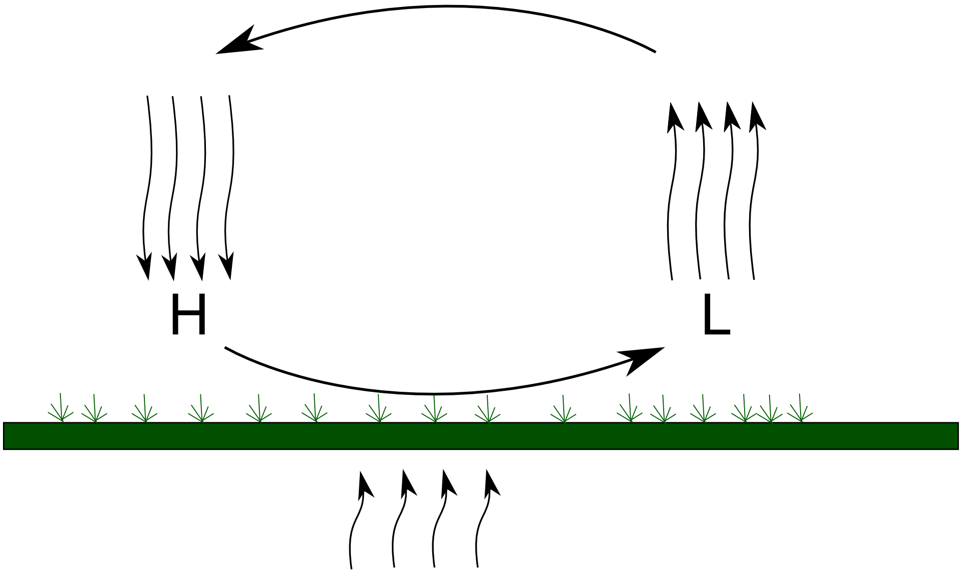

Figure 2.1: A simple convection cell, with low pressure denoted by L and high pressure by H.

## 2.2 Global wind patterns

As mentioned in the previous section the heat energy from the sun is spread unevenly across the earths surface causing unbalance in the energy system of the earth. At the same time the earth continuously radiates thermal energy back into space. This results in a negative energy budget at the poles and at higher latitudes and a positive budget at lower latitudes [Emeis, 2013]. In order to balance this system, the earth transports vast amounts of heat from equatorial latitudes to the poles. This complex heat transportation system makes up the global climate and consists of circulations in the oceans and atmosphere as well as direct transportation of energy through heat conduction [Emeis, 2013].

There are three main convection cells making up the global wind system [Boyle, 2004], seen in Figure 2.2. Description of these cells will only be given for the northern hemisphere, as they are mirrored for the Southern Hemisphere.

The first cell, the Hadley cell, goes from about 0 degrees to about 30 degrees latitude. At equator the earth's surface consist to a large extent of oceans. Being also the latitude of which most solar energy is incident on a given surface area, a low pressure belt is created consisting of a cloudy, warm and humid climate. This is the result of huge amounts of water evaporating from the oceans to the atmosphere. As the air is heated up the now humid air will expand and rise up into the atmosphere until it reaches the tropopause [Boyle, 2004].

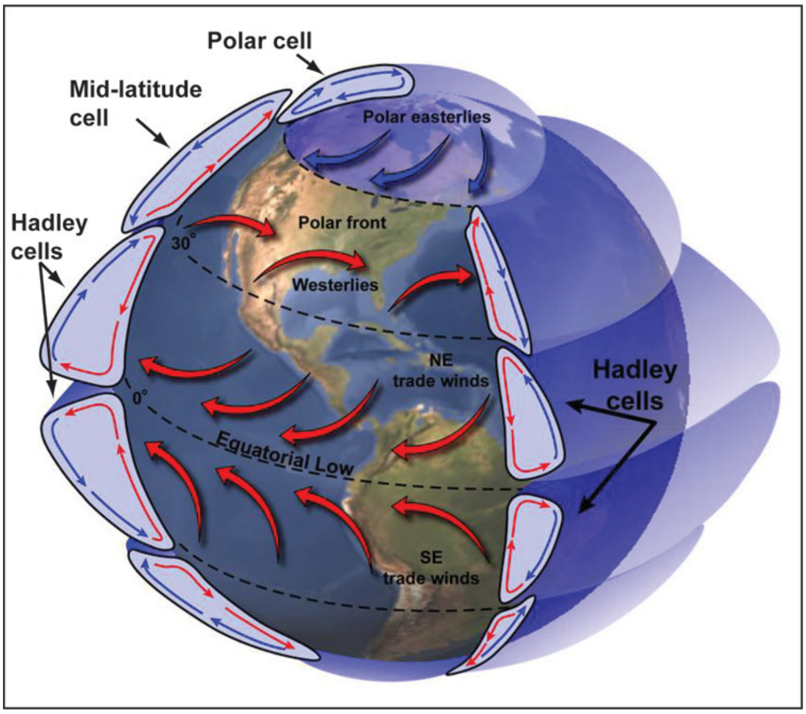

Figure 2.2: The global wind circulation [Guido, 2008].

While the air rises up, it cools and much of the water content in the air will start to condensate into clouds. These clouds will work as a blanket covering the equator and reflect the incoming solar radiation, thus actually contributing to less solar radiation reaching the surface at equator. As the air rises to the tropopause, the air will move towards the poles, i.e. northwards in the Northern Hemisphere and southwards in the Southern Hemisphere [Boyle, 2004]. The air will keep on cooling until it reaches about 30 degrees latitudes. At this point the air has become so dense that it will start sinking down towards the surface. This air is now dry, cold and dense, creating a high pressure belt, as seen in Figure 2.2, being why many of the earth's deserts are found at 30 degrees latitudes. Parts of the air at the surface will now be forced towards the low pressure belt at equator, completing the air circulation between 0 and 30 degrees latitudes. This is known as the Hadley cell.

The remaining air will be forced towards the poles, and will continue to move until it reaches the polar front. At this point the lower latitude air will be warmer than that which comes from the poles, thus lower latitude air rises up to about 60 degrees latitude, creating another low pressure belt around the planet. Again one part of this air will move towards equator, more specifically towards 30 degrees latitude, completing the second convection cell, i.e. the Ferrel cell. The second part will move towards the poles, until it cool down at higher latitudes, which lead to the third and last cell, namely the Polar cell [Boyle, 2004]. This is the reason for the high pressure at the poles, and since the air at high latitudes are much colder than that of lower latitudes, it can hold less water. These polar latitudes are, like the 30 degrees latitude, also characterized by desert areas.

However, as stated by Emeis [2013], these cells would only create a meridional wind pattern. In order to get a more realistic picture of the global wind patterns, the earth's rotation must be included. The earth is rotating from west to east, or as seen from the North Pole, counter-clockwise. As a result of this, the winds moving towards the poles will get a westerly velocity component, while the winds moving towards the equator will get a easterly velocity component. This is the effect of a pseudoforce known as the Coriolis effect. These components give rise to the well known wind patterns as westerlies, polar easterlies and the trade winds, seen in Figure 2.2.

## 2.3 Vertical wind speed profile

When discussing the vertical wind speed profile with respect to wind turbines Emeis [2013] first considers a flat horizontally homogeneous atmospheric boundary layer (ABL). This layer is the lower part of the Troposphere and the lowest layer of the atmosphere. According to Emeis [2013] the atmospheric boundary layer can be divided into three principal types

1. Neutral boundary layer: in this layer the heat flux at the lower surface is negligible and the layer are instead dominated by dynamical shear forces.

2. Unstable boundary layer: this layer is dominated by heat input from below causing a convective (unstable) boundary layer.

3. Stable boundary layer: when the atmosphere is cooled from below the boundary layer is said to be stable.

Figure 2.3 shows the vertical stratification of a ABL with the Ekman, Prandtl and roughness sublayers illustrated with their corresponding order of heights. Two wind turbines are also illustrated as a reference to the layer heights. Both turbines have a hub height of 80 meter and a rotor diameter of 90 meter, which is the dimensions given for the V90-3.0MW located at Fakken wind farm [Vestas Wind Systems A/S, 2013]. The left hand side is illustrated relative to a $z_i$ = 1000 m, which will result in the Prandtl layer going up to 100 meters, and the right hand side wind turbine relative to $z_i$ = 2500 m. It should be noted that in the left hand case the tip height of the wind turbine extends into the Ekman layer, whereas for the right hand case the tip height is within the Prandtl layer with good margins.

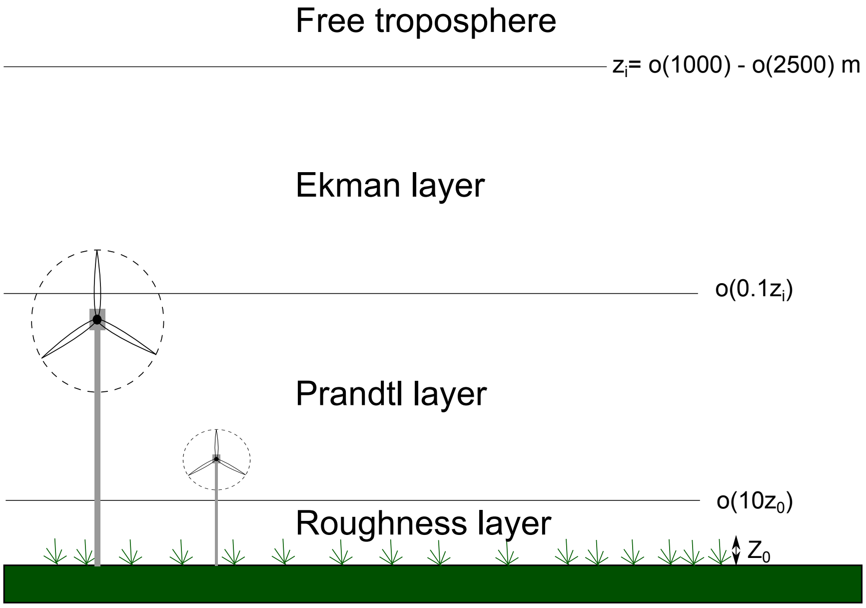

Figure 2.3: Vertical layers of the atmospheric buondary layer over flat homogenous terrain.

As meteorology is not the main focus of this study, only a short summary of the various layers within the ABL and the corresponding vertical wind profile laws will be given in the following sections. More detailed information on this subject is given in [Emeis, 2013] and the pre-study for this thesis [Jacobsen, 2013].

The Prandtl layer, also known as the surface layer, is the layer between the Ekman and roughness layers. As seen in Figure 2.3 this layer usually makes up 10 % of the ABL. Since the Prandtl is so close to the surface, the affect from the Coriolis force can be neglected and meteorologically the layer is defined as where the turbulent vertical fluxes of moisture, heat and momentum differs from their surface values with only 10 % [Emeis, 2013]. In the Ekman layer the wind profile is influenced by three forces, (i) the Coriolis force, (ii) the pressure gradient force and (iii) the frictional forces.

### 2.3.1 Logarithmic law

The vertical wind speed gradient, also known as the wind shear, in the Prandtl layer in the case of neutral stratification is given as Emeis [2013]

$$\frac{\partial u}{\partial z} = \frac{u_*}{l} = \frac{u_*}{\kappa z}, \tag{2.1}$$

where $u$ is the wind speed, $z$ the height, $u_*$ the friction velocity, $l$ the mixing length and $\kappa = 0.4$ is the Kármán constant

It is then possible to derive an expression for the wind speed as a function of height by integrating Equation 2.1 from the lower height $z_0$ (roughness length), where the wind speed is assumed to vanish near the ground, up to a height $z$ within the Prandtl layer

$$\begin{aligned}
\int_0^u \mathrm{d}u &= \int_{z_0}^{z} \frac{u_*}{\kappa z}\,\mathrm{d}z \\
&= \frac{u_*}{\kappa}\int_{z_0}^{z} \frac{1}{z}\,\mathrm{d}z \\
&= \frac{u_*}{\kappa}(\ln z - \ln z_0) \qquad (2.2) \\
&= \frac{u_*}{\kappa}\ln\frac{z}{z_0} \\
\Rightarrow u(z) &= \frac{u_*}{\kappa}\ln\frac{z}{z_0}.
\end{aligned}$$

However, rarely is the thermal stratification of the Prandtl layer found to be absolutely neutral. For unstable and stable stratifications a correction function must therefore be added to Equation 2.2 so it becomes [Emeis, 2013]

$$u(z) = \frac{u_*}{\kappa}\left(\ln\left(\frac{z}{z_0}\right) - \Psi_m\left(\frac{z}{L_*}\right)\right), \tag{2.3}$$

where $L_*$ is the Obukhov length defined as

$$L_* = \frac{\theta_v}{kg}\frac{u_*^3}{\overline{\theta_v' w'}}. \tag{2.4}$$

Here $u_*$ is the friction velocity, $\theta_v$ the potential temperature, $g$ the gravitational acceleration and $\overline{\theta_v^{‘} w^{‘}}$ is the virtual heat flux. The Obukhov length is negative for unstable stratification and positive for stable stratification. More details regarding the Obukhov length can be found in [Emeis, 2013].

In the case of unstable stratification the correction function becomes

$$\Psi_m = 2\ln\left(\frac{1+x}{2}\right) + \ln\left(\frac{1+x^2}{2}\right) - 2\arctan(x) + \frac{\pi}{2}, \tag{2.5}$$

where $x = (1 - bz/L_*)^{1/4}$ [Paulson, 1970] and $b = 16$ [Emeis, 2013]. For stable stratification the correction function becomes

$$\Psi_m = \begin{cases} -a(z/L_*) & \text{for } 0 < z/L_* \leq 0.5 \\ A(z/L_*) + BC/D + ... & \\ B\,(z/L_* - C/D)\exp\left(-D(z/L_*)\right) & \text{for } 0.5 \leq z/L_* \leq 7, \end{cases} \tag{2.6}$$

with a = 5, A = 1, B = 2/3, C = 5 and D = 0.35 [Emeis, 2013].

### 2.3.2 Power law

The power law is an empirical law used to describe the vertical wind profile. It is often preferred to the logarithmic law due to its mathematically simplicity and it is defined as [Emeis, 2013]

$$u(z) = u(z_r)\left(\frac{z}{z_r}\right)^a. \tag{2.7}$$

The Hellman exponent $a$ depends on the surface roughness and the thermal stability of the Prandtl layer and $z_r$ is the reference height.

## 2.4 Distribution of wind

### 2.4.1 Weibull distribution

The Weibull distribution is a common function used to model how the occurrences of wind speeds are distributed [Seguro and Lambert, 2000]. In a early study by Justus et al. [1976] this distribution was seen to fit well with the observed wind speed data measured at various sites across the continental United States.

For a random Weibull distributed variable $U \sim W(a,b)$ , Conradsen et al. [1984] describes the following statistical characteristics:

**Probability density function**

$$f(u;a,b) = \frac{b}{a}\left(\frac{u}{a}\right)^{b-1}\exp\left(-\left(\frac{u}{a}\right)^b\right), \quad u \geq 0, \tag{2.8}$$

**Cumulative distribution function**

$$F(u;a,b) = 1 - \exp\left(-\left(\frac{u}{a}\right)^b\right), \quad u \geq 0, \tag{2.9}$$

**Mean**

$$E(U) = \mu = a\Gamma\left(1 + \frac{1}{b}\right), \tag{2.10}$$

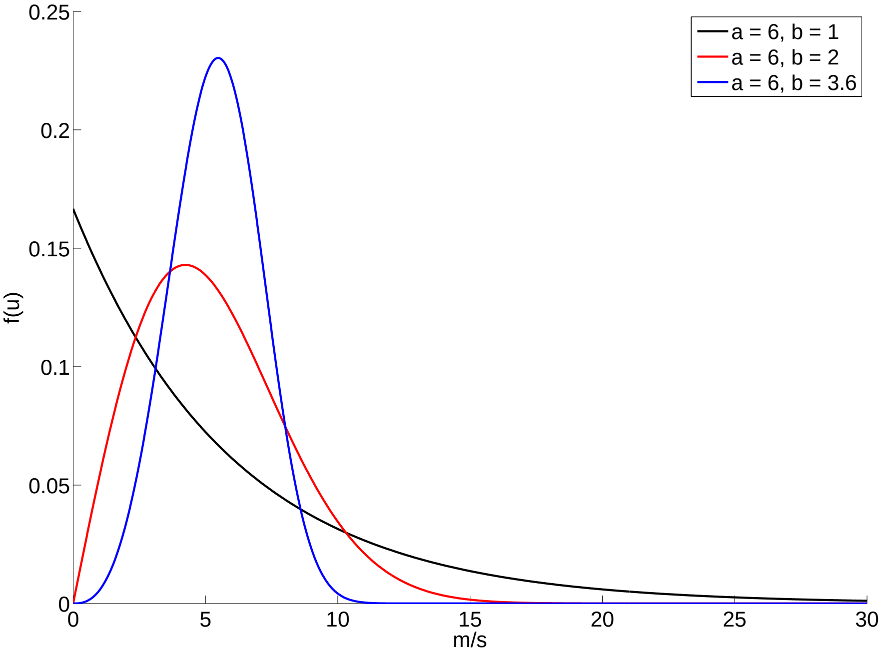

Figure 2.4: Weibull probability density function as a function of wind speed for various values of $b$.

### Variance

$$Var(U) = \sigma^2 = a^2 \left( \Gamma \left( 1 + \frac{2}{b} \right) - \Gamma^2 \left( 1 + \frac{1}{b} \right) \right), \tag{2.11}$$

where $\Gamma()$ is the gamma function. For $b = 1$ the distribution is an exponential distribution with mean value $a$, while $b = 2$ gives a Rayleigh distribution. When $b = 3.6$ the distribution approaches the Gaussian distribution [Conradsen et al., 1984]. Figure 2.4 show some examples of the probability density function with various parameter values.

Seguro and Lambert [2000] describes three methods for estimating $a$ and $b$ of the Weibull distribution: (i) the maximum likelihood method, (ii) the modified maximum likelihood method and (iii) the graphical method. Methods (i) and (ii) are described as follows:

### The maximum likelihood method

Consider a set of $n$ measurements of non-zero wind speeds $u$, where $u_i$ is the wind speed at time step $i$. The parameters $a$ and $b$ can then be estimated as

$$a = \left( \frac{1}{n} \sum_{i=1}^{n} u_i^b \right)^{\frac{1}{b}}, \tag{2.12}$$

$$b = \left( \frac{\sum_{i=1}^{n} u_i^b \ln(u_i)}{\sum_{i=1}^{n} u_i^b} - \frac{\sum_{i=1}^{n} \ln(u_i)}{n} \right)^{-1}, \tag{2.13}$$

where Equation 2.13 must be solved before Equation 2.12, using an iterative procedure of which a suitable initial guess is $b = 2$ [Seguro and Lambert, 2000]. This is known as the maximum likelihood method.

### The modified maximum likelihood method

In the case that the wind speed data are given in frequency distribution format, i. e. the data are sorted into equally sized bins corresponding to wind speed intervals, such as for instance used when representing data in a histogram, a modified version of the maximum likelihood method can be applied instead using the following equations [Seguro and Lambert, 2000]

$$a = \left( \frac{1}{P(u \geq 0)} \sum_{i=1}^{n} u_i^b P(u_i) \right)^{\frac{1}{b}}, \tag{2.14}$$

$$b = \left( \frac{\sum_{i=1}^{n} u_i^b \ln(u_i) P(u_i)}{\sum_{i=1}^{n} u_i^b P(u_i)} - \frac{\sum_{i=1}^{n} \ln(u_i) P(u_i)}{P(u \geq 0)} \right)^{-1}, \tag{2.15}$$

where $n$ now is the number of bins which the data are sorted into and $u$ is still the wind speed, while $u_i$ is the wind speed central to bin $i$. $P(u_i)$ is the probability of wind speed $u$ falling within the intervals of bin $i$ and $P(u \geq 0)$ is the probability that the wind speed is equal or greater than zero. Like before, Equation 2.15 must be solved iteratively before an explicitly solution for $a$ using Equation 2.14 can be obtained.

The Weibull parameters $a$ and $b$ are related to the average wind speed by [Seguro and Lambert, 2000]

$$\bar{u} = a\Gamma\left(1 + \frac{1}{b}\right), \tag{2.16}$$

where $\mathit{\Gamma}()$ is the gamma function.

## 2.4.2 Alternative distributions

In a recent study by Drobinski and Coulais [2012] the authors questions the general suitability of the Weibull distribution to describe the wind speed distribution and thus the wind power evaluation at a site. In their article data from four different sites in France were evaluated. These showed that for the site with relatively flat terrain and isotropic winds, the distribution of the wind could be fairly well described using the Weibull distribution. For the three remaining sites with more complex terrain and anisotropic wind however, the Weibull distribution did not very well describe the wind distribution. According to Drobinski and Coulais [2012] the reason for this was assumed to be that the area for the three remaining sites had two wind regimes: (1) random flow: wind components have zero means and same variance and (2) channeled flow: wind components have different means. The wind statistics of the first regime is well described by the Rayleigh distribution and the second regime by the Rice distribution. A Rayleigh-Rice distribution, given by Equation 2.17 which takes into account the wind components instead of only the wind speed was therefore proposed to be used. This gave a much lower relative error for the complex sites compared to the Weibull distribution. This may suggest that how well the Weibull distribution fits the wind speed distribution varies with features such as the complexity of the terrain and whether the wind is isotropic or anisotropic.

$$\begin{aligned} p_M(M;\mu,\sigma^2,\alpha) = & \frac{M}{Z}\exp\left(-\frac{M^2}{2\sigma^2}\right)\times \\ & \left(\alpha+(1-\alpha)\exp\left(-\frac{\mu^2}{2\sigma^2}\right)I_0\left(\frac{M\mu}{\sigma^2}\right)\right), \end{aligned} \tag{2.17}$$

where $M = \sqrt{u^2+v^2}$ is the wind velocity with wind speed components $u$ and $v$, $I_0()$ is the modified Bessel function of the first kind and zero order, $\alpha$ the weight corresponding to channeled flow events occurrence and $Z = \int p_M(M;\mu,\sigma^2,\alpha)\mathrm{d}M$ is the normalization factor [Drobinski and Coulais, 2012].

## 2.5 Wind power production

### 2.5.1 Energy in the wind

Wind energy is the kinetic energy of air in motion. As described by Boyle (2004) this kinetic energy is defined as

$$E_k = \frac{1}{2}mu^2, \tag{2.18}$$

where $m$ is the mass of moving air and $u$ its velocity, in kilograms and meters per second respectively.

Considering a cross-sectional area $A$ being perpendicular to the wind direction of $u$, the volumetric flow rate of the air $Q$, i.e. the volume of air $V$ flowing through $A$ per unit time $t$, can be expressed as

$$Q = \frac{\mathrm{d}V}{\mathrm{d}t} = uA. \tag{2.19}$$

Starting with the definition of power it is possible to derive an expression for the power available in the wind.

$$\begin{aligned} P &= \frac{\mathrm{d}W}{\mathrm{d}t} \\ &= \frac{E_k}{t} \\ &= \frac{\frac{1}{2}mu^2}{t} \\ &= \frac{1}{2}\frac{m}{t}u^2\frac{V}{V} \\ &= \frac{1}{2}\frac{m}{V}u^2\frac{V}{t} \\ &= \frac{1}{2}\rho u^2 Q \\ &= \frac{1}{2}\rho u^2(uA) \\ &= \frac{1}{2}\rho A u^3, \end{aligned} \tag{2.20}$$

where $\rho$ is the density of the air. In other words, the power in the wind is proportional to the third order of the wind speed $u$.

However, as noted by Andrews and Jelley [2007], all of this power cannot be extracted using a wind turbine. This has to do with the fact that some kinetic energy is needed in order to maintain an air flow through the wind turbine. The wind turbine will convert the kinetic energy to mechanical energy, thus slowing down the wind speed. If the wind is slowed down completely, the air flow through the turbine would cease and so would the power extraction.

### Betz limit

Using momentum theory it is possible to make an estimate of the maximum efficiency of power extraction from the wind using a wind turbine [Andrews and Jelley, 2007]. First consider the stream-tube seen in Figure 2.5. Starting with speed $u_0$ the wind flow upstream pass through a cross-sectional area $A_0$ As it reaches the wind turbine, the area of the steam-tube of air increases to $A_1$ and as a result the wind speed will be decreased to $u_1$. Some of the kinetic energy of the air will be converted to mechanical energy in the rotor, reducing the wind speed further in addition to the effect from the increased area of the stream-tube downstream.

There are two ways to express the power extracted by the wind turbine [Andrews and Jelley, 2007]. First as the loss of kinetic energy per unit time as the wind flow through the turbine

$$\begin{aligned} P &= P_{\text{upstream}} - P_{\text{downstream}} \\ &= \frac{E_{k0}}{\mathrm{d}t} - \frac{E_{k2}}{\mathrm{d}t} \\ &= \frac{1}{2}\frac{\mathrm{d}m}{\mathrm{d}t}u_0^2 - \frac{1}{2}\frac{\mathrm{d}m}{\mathrm{d}t}u_2^2 \\ &= \frac{1}{2}\frac{\mathrm{d}m}{\mathrm{d}t}\left(u_0^2 - u_2^2\right). \end{aligned} \tag{2.21}$$

Second expression is obtained by looking at the change of momentum. Consider the rotor as a actuator disc, i.e. a thin disc that extracts energy. As the wind speed drop when the wind flow passes through the turbine, a pressure drop will occur [Andrews and Jelley, 2007]. Bernoulli's theorem states that for an ideal fluid, the energy must be conserved. Assuming the air is an ideal fluid, it is possible to use Bernoulli's equation to find the trust, T, exerted on the turbine blades which again will lead to the power extracted. The Trust is given by

$$\begin{aligned} T &= u\frac{\mathrm{d}m}{\mathrm{d}t}(\Delta u) \\ &= \frac{\mathrm{d}m}{\mathrm{d}t}(u_0 - u_2), \end{aligned} \tag{2.22}$$

where $T$ is the thrust force and $\mathrm{d}m/\,\mathrm{d}t$ the rate of which the mass of air flow through the stream-tube. The extracted power as a function of the thrust can now be expressed as

$$\begin{aligned} P &= Tu_1 \\ &= \frac{\mathrm{d}m}{\mathrm{d}t}\left(u_0 - u_2\right)u_1. \end{aligned} \tag{2.23}$$

Combining Equation (2.21) and Equation (2.23), an expression for $u_1$ and $u_2$ can be obtained by

$$\begin{aligned} \frac{\mathrm{d}m}{\mathrm{d}t}\left(u_0 - u_2\right)u_1 &= \frac{1}{2}\frac{\mathrm{d}m}{\mathrm{d}t}\left(u_0^2 - u_2^2\right) \\ \left(u_0 - u_2\right)u_1 &= \frac{1}{2}\left(u_0^2 - u_2^2\right) \\ u_1 &= \frac{1}{2}(u_0 + u_2) \\ u_2 &= 2u_1 - u_0. \end{aligned} \tag{2.24}$$

and the mass flow per second can be rewritten as [Andrews and Jelley, 2007]

$$\frac{\mathrm{d}m}{\mathrm{d}t} = \rho u A = \rho u_1 A_1. \tag{2.25}$$

Using Equations (2.24) and (2.25), Equation (2.23) becomes

$$\begin{aligned} P &= (\rho u_1 A_1)\,(u_0 - (2u_1 - u_0))\,u_1 \\ &= 2\rho u_1^2 A_1 (u_0 - u_1). \end{aligned} \tag{2.26}$$

Define an induction factor $a$, so that

$$a = \frac{u_0 - u_1}{u_0}, \tag{2.27}$$

and a power coefficient $C_p$ as

$$\begin{aligned} C_p &= \frac{P}{\frac{1}{2}\rho u_0^3 A_1} \\ &= 4a(1-a)^2, \end{aligned} \tag{2.28}$$

which is the ratio between the power in the wind and the power extracted by the turbine. It is then possible to find the solution for $a$ which will yield the maximum power extraction as follows

$$\begin{aligned} \frac{\mathrm{d}C_p}{\mathrm{d}t} &= 0 \\ \frac{\mathrm{d}}{\mathrm{d}t}\left(4(1-a)^2\right) &= 0 \\ 12a^2 - 16a + 4 &= 0, \end{aligned} \tag{2.29}$$

which is on the form of a quadric equation that can be solved using the quadric formula resulting in the two solutions

$$a = \begin{cases} 1 \\ \frac{1}{3} \end{cases}. \tag{2.30}$$

For $a = 1$, $P = 0$, and the maximum power is therefore found for the solution $a = 1/3$, or the equivalent $u_1 = (2/3)u_0$ . Using Equation (2.28) the limit for the power coefficient can be found as

$$\begin{aligned} P_{\text{max}} &= \frac{1}{2}\rho u_0^3 A_1 \left(4\left(\frac{1}{3}\right)\left(1 - \frac{1}{3}\right)^2\right) \\ &= \frac{1}{2}\rho u_0^3 A_1 \left(\frac{16}{27}\right) \\ &= P_{wind} C_p. \end{aligned} \tag{2.31}$$

In other words, the maximum ratio of power which can be extracted by the wind turbine, $P_{max}$, of the power in the wind incident on the turbine, $P_{wind}$, is given by the power coefficient $C_p$. This limit is called Betz limit and is approximately 59 % [Andrews and Jelley, 2007].

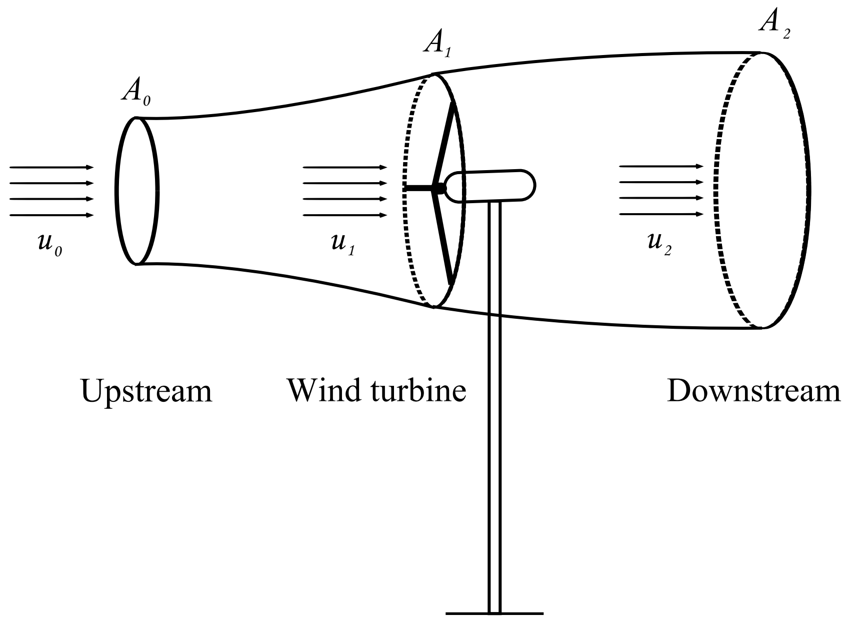

Figure 2.5: Airflow through a HAWT.

### 2.5.2 Wind turbine blade design

The blades of a modern wind turbine are most commonly shaped like an airfoil, reason being that the shape allows for efficient extraction of the energy in the wind [Mathew, 2006]. It is therefore natural to first look at how lift is created on an airfoil and a good review on this is given by Babinsky [2003].

Consider the airfoil seen in Figure 2.6. The white lines seen are smoke particles flowing along a lifting airfoil section [Babinsky, 2003]. To the left in Figure 2.6a the streamlines are seen to be undisturbed by the airfoil, however as the smoke particles approaches the airfoil the streamlines curves around the airfoil as seen in Figure 2.6b and Figure 2.6c. This happens because the shape of the airfoil induces curvature into the flowfield and the flow will follow the local curvature of the upper and lower surfaces, which again is a result from friction between the airfoil and the particles.

As noted by [Babinsky, 2003], in order for the streamlines to be curved, there must be a force acting on the particles normal to the direction of motion. This force origins from pressure gradients and for the case seen in Figure 2.6 the pressure above the airfoil will be lower than the normal atmospheric pressure, while at the lower side of the airfoil the pressure will be greater. These pressure gradients are greater closer to the surface, as seen in the figure. Note also that the air particles moving above the airfoil moves faster than the ones below. This can be explained by Bernoulli's law which states that the decrease in pressure of an inviscid flow will result in

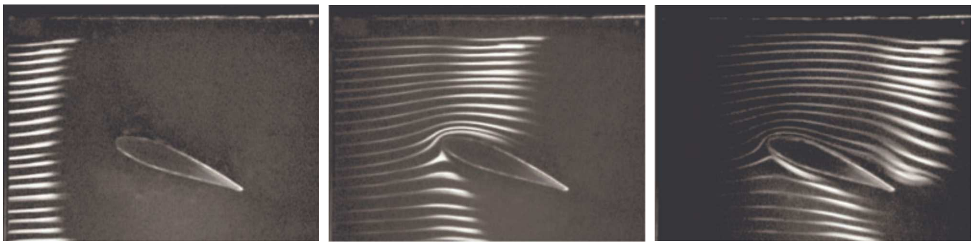

(a) (b) (c)

Figure 2.6: Air particles flowing along an airfoil [Babinsky, 2003].

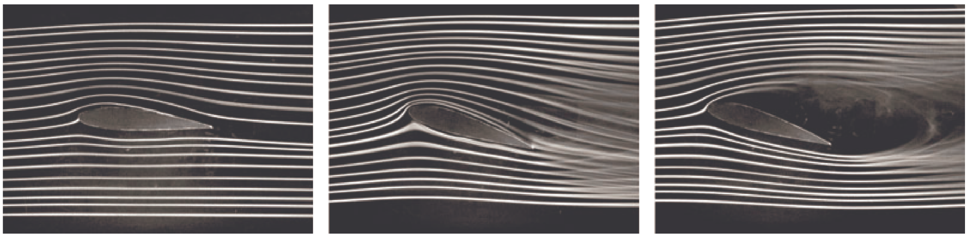

(a) Low angle of attack (b) High angle of attack (c) Stalled flow

Figure 2.7: Streamlines flowing along an airfoil with increased angle of attack [Babinsky, 2003].

an increased speed of the fluid, vice versa [Giancoli, 2005].

Figure 2.7 shows how the streamlines around an airfoil are affected by the angle of attack. For low angle of attack, as seen in Figure 2.7a, the streamlines are less densely packed around the surface of the airfoil compared to Figure 2.7b. This implies that there is more lift generated for a higher angle of attack. If the angle is increased too much however, the flow above the airfoil will no longer be able to follow the sharp curvature of the airfoil, resulting in the sharp drop-off in the lift force seen in Figure 2.7c [Babinsky, 2003].

Mathew [2006] divides the force exerted on the wind turbine blade into two components: The lift force $L$, which is the force perpendicular to the direction of the undisturbed flow, and the drag force $D$, which is the force exerted in the same direction as the undisturbed flow. These forces are seen in Figure 2.8b, which illustrates a section of one of the blades at a length $r$ from the rotor center of the wind turbine seen in Figure 2.8a. The wind incident on the turbine has a speed $u_1$ and the blade a rotational speed $v$, perpendicular to the direction of the air flow.

The lift and drag forces are given as [Mathew, 2006]

$$L = C_L \frac{1}{2} \rho_a A_1 u_1^2, \tag{2.32}$$

and

$$D = C_D \frac{1}{2} \rho_a A_1 u_1^2, \tag{2.33}$$

respectively, where $C_L$ and $C_D$ are the corresponding lift and drag coefficients, $\rho_a$ is the air density, $A_1$ the cross-sectional area of the turbine and $u_1$ the incident wind speed.

For a turbine blade with maximum radius $R$, the speed of the blade at a radius $r$ from the center of the rotor is given by Andrews and Jelley [2007] to be

$$v = \frac{r v_{tip}}{R}. \tag{2.34}$$

Using trigonometric properties, the following relation can be derived from Figure 2.8b

$$\tan(\phi) = \frac{u_1}{v}, \tag{2.35}$$

where $\phi$ is the angle between $v$ and the resultant speed of the air relative to the blade, $u_\alpha$.

Neglecting the drag force, Andrews and Jelley [2007] derives an expression for the power as a function of the lift force as follows

$$\begin{aligned} P &= Fv \\ &= L(\sin(\phi))v \\ &= L(\sin(\phi))\frac{u_1}{\tan(\phi)} \\ &= L(\cos(\phi)u_1 \\ &= Tu_1, \end{aligned} \tag{2.36}$$

which implies that the power developed equals the power delivered by the thrust force, as was seen in Equation 2.23.

Another critical parameter which should also be considered is the tip-speed ratio $\lambda$, defined by Andrews and Jelley [2007] as

$$\lambda = \frac{v_{tip}}{u_0}, \tag{2.37}$$

where $v_{tip}$ is the speed of the blade tip and $u_0$ the wind speed incident on the cross-sectional area $A_0$, as seen in Figure 2.5.

Combining Equations 2.37 and 2.34 with Equation 2.35 yields

$$\tan(\phi) = \frac{u_1}{v} = \frac{2R}{3r\lambda}, \tag{2.38}$$

where the Betz condition $u_1 = (2/3)u_0$ has been used. From this result it is possible to observe that the angle $\phi$ only depends on the tip-speed ratio for a given radius $r$. As increased radius $r$ implies that the angle $\phi$ will decrease, modern wind turbine blades are design with a twist which increases with decreasing $r$. By doing so the optimal angle of attack are obtained over the whole turbine blade. Modern blades are also design so that the width $W$ decreases with increased radius $r$. This is to make the lift components generate the required thrust for the Betz condition to be maintained [Andrews and Jelley, 2007].

### 2.5.3 Horizontal axis wind turbine design

Like the majority of wind turbine designs today, the wind turbines installed at Fakken wind farm are HAWTs [Andrews and Jelley, 2007]. A detailed illustration of the various components included in a modern HAWT is shown in Figure 2.9. The rotor consists of a hub, typically with three turbine blades shaped like airfoils attached to it. This is also the case for the Vestas V90 3.0 MW wind turbines installed at Fakken wind farm, which have rotor diameters of 90 meter [Vestas Wind Systems A/S, 2013]. Each blade can be rotated, known as pitching the blade, in order to most efficiently harvest the wind energy and when the wind speed is too high, reduce the fatigue on the blade.

On top of the tower is the nacelle which encloses most of the important components of a wind turbine. As can be seen in the illustration, the rotor is attached to the nacelle. Closest to the rotor lies the break whose main function is to be a backup to the breaking effect obtained by pitching the blade and work as a parking break when conducting maintenance. A low-speed shaft is used to transfer the mechanical energy from the rotor, by a gear box, to a high-speed shaft attached to a generator. For large turbines, the low-speed shaft will typically have 20 revolutions per minute (rpm) and by using the gear box this speed can be increased to about 1200 - 1800 rpm for the high-speed shaft [Schubel and Crossley, 2012]. The increased speed makes it possible to convert the mechanical energy from the rotor into electricity using the generator.

Next to the generator is a heat exchanger, which keeps the generator cool, and a control unit. As the weather conditions such as wind speed and direction are constantly changing it is very important to find the most ideal settings for the wind turbine to ensure the highest electricity production. The controller have a computer system which takes care of this. This system can run self-diagnostic tests, start and stop the turbine as well as make adjustment with regards to the pitching of the blades and the direction of the nacelle using the yaw drive.

For the controller to find the most ideal settings, it requires some input data. An anemometer and a wind vane are therefore placed on top of the nacelle, passing along data regarding the wind speed and wind direction respectively.

The two last components seen in the wind turbine illustration in Figure 2.9 are the yaw drive and the tower. The nacelle can be turned using the yaw

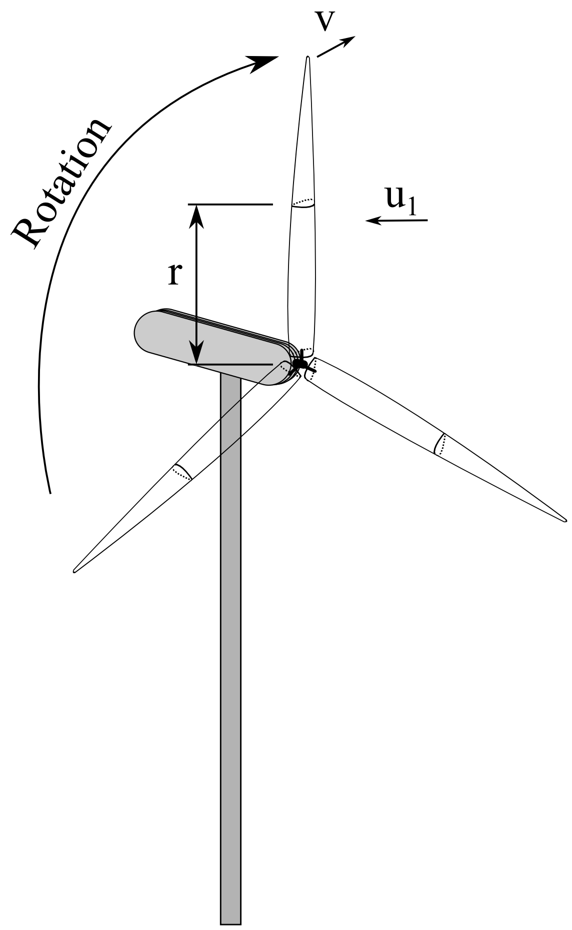

(a) HAWT.

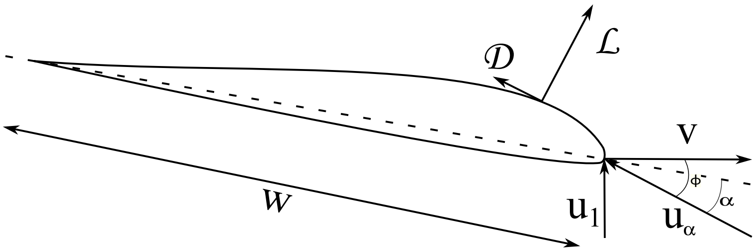

(b) Turbine blade section.

Figure 2.8: Wind incident on a horizontal axis wind turbine (a), with a section of a turbine blade at length $r$ from the rotor center given in (b).

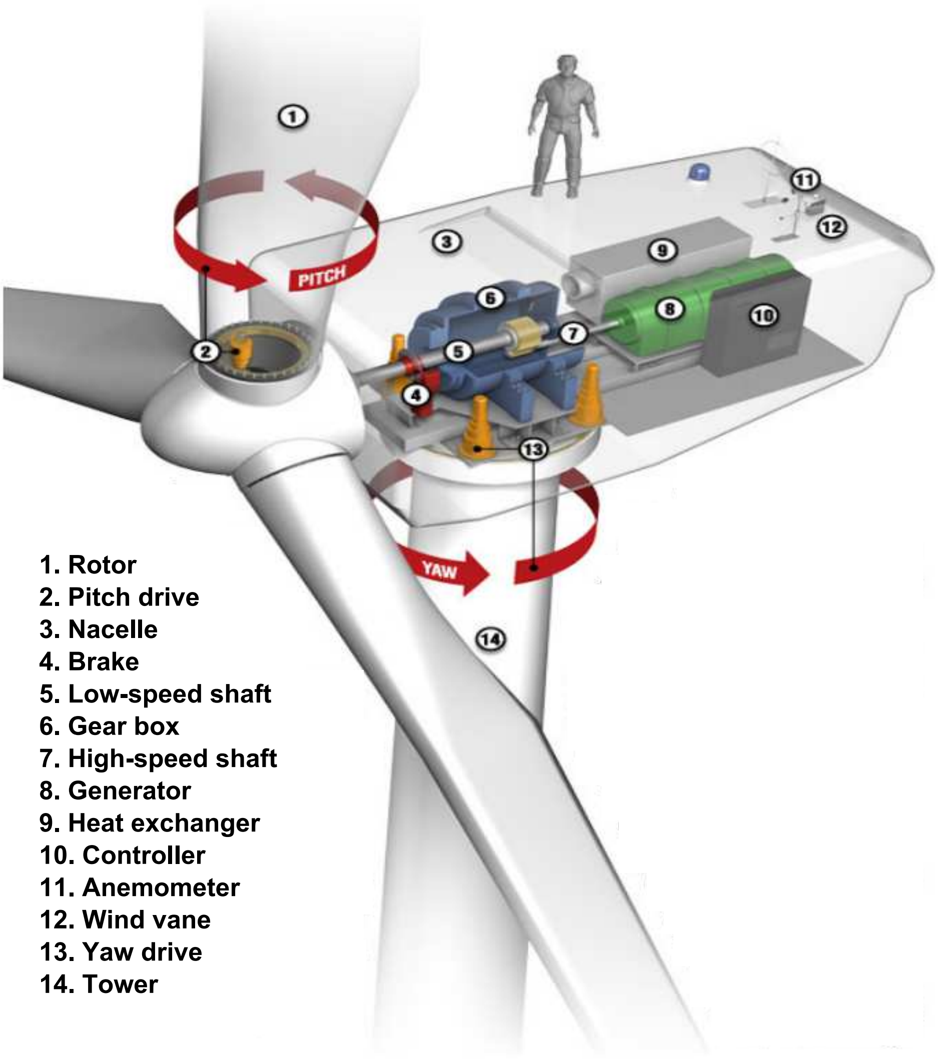

Figure 2.9: Design of a modern HAWT [Schubel and Crossley, 2012].

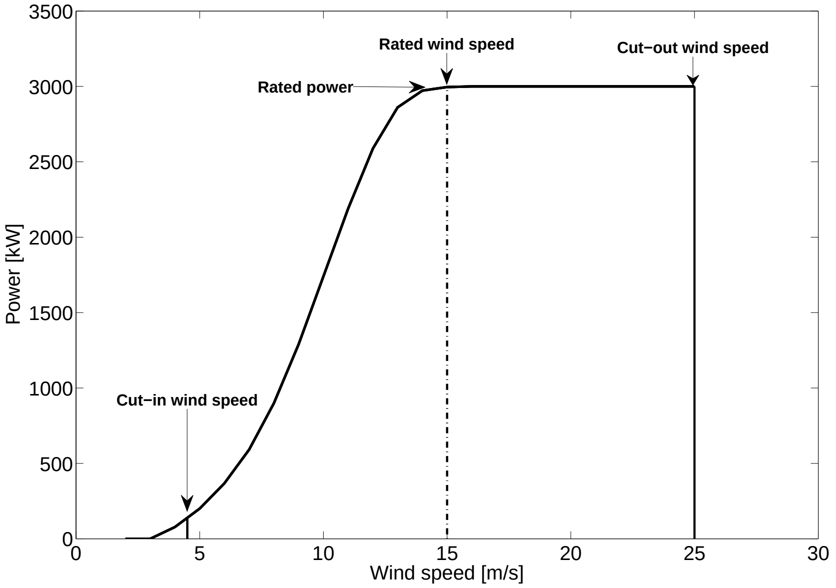

Figure 2.10: Power curve showing the relation between output power and wind speed for a Vestas V90 3.0MW HAWT. Values in graph are taken from [Vestas Wind Systems A/S, 2013].

drive, keeping the rotor facing the wind. As wind speed generally increases with height, the height of the tower corresponds to how much of the wind energy the turbine are able to capture. The wind turbines at Fakken have a hub height of 80 meters [Vestas Wind Systems A/S, 2013].

### 2.5.4 Power curve

The power curve of a wind turbine shows the expected output power of the turbine as a function of wind speed. This curve is unique for every type of wind turbine and can be used to find the most suitable type of turbine for a given site. A typical power curve is seen in Figure 2.10, which shows the power curve for the Vestas V90-3. 0 MW HAWT [Vestas Wind Systems A/S, 2013].

The rotor starts rotating when the wind speed reaches the *cut-in wind speed* at 3.5 m/s. At 15 m/s, *rated wind speed*, the maximum output power is generated by the turbine and this continues up to 25 m/s which is the *cut-out wind speed.* This is a safety limit set to avoid great loads and fatigue on the turbine. At this point the rotor is slowed down either by changing the pitch of the blades which will reduce the angle of attack, by the design of the blade or by applying the shaft brake [Andrews and Jelley, 2007].

## 2.6 Topographic features

### 2.6.1 Wake effects

When wind traverse through a wind turbine some of its kinetic energy will be converted to electrical energy. As a result, the wind at the lee side of the turbine will have a lower speed and energy content than the wind upstream of the turbine [Koch et al., 2005]. In addition to a reduced speed, the wind downstream of the turbine will also be turbulent. This downstream wind is known as the wake of the turbine and according to González-Longatt et al. [2012] these two features are the main effects of a wake.

For a wind farm, the reduced wind speed downstream will affect the energy production from downwind turbines negatively. These turbines are said to be shadowed by the wake producing turbine. According to Koch et al. [2005] the total energy production from a wind farm is reduced by a few percentage as a result of this wake effect. Additionally the increased turbulence of the wind may result in increased dynamic mechanical loads on the downward turbines [González-Longatt et al., 2012].

In order to maximize the energy production from a wind farm, thus increasing the efficiency of the farm, it is very important to understand and minimize the wake effects when designing wind farms. A numerous selection of both simple and complex models have been developed to simulate these wake effects, of which two of them are described by Koch et al. [2005] and González-Longatt et al. [2012].

### 2.6.2 Mountain waves

Mountain waves are a feature of mesoscale meteorology which occur when stable stratified air is forced to flow over sinusoidally varying surface topography, for instance mountains [Holton and Hakim, 2012]. These mountain waves are divided into two categories: (i) the vertically propagating and (ii) the vertically decaying.

Figure 2.11 shows vertically propagating mountain waves. A upstream phase tilt occur when the streamlines flow over the mountain ridge which propagates vertically. In this case the mean cross mountain wind speed is not increasing significantly and the stability of the stratification increases with height. The pattern is periodic with height and if enough moisture is present orographic clouds may develop in the regions where the streamlines are displaced, both upstream and downstream of the ridge [Holton and Hakim, 2012] as can be observed in Figure 2.11.

However, if the stability of the layers decreases strongly with height and the mean cross mountain wind speed increases strongly with height, the vertically propagating waves in the lower layer will be reflected when they reach the upper layer. If this occur repeatedly the result becomes so called trapped lee waves as can be seen in Figure 2.12.

Under some conditions partial reflection of the vertical propagating waves can also produce strong surface winds along the lee slopes of mountain ranges [Holton and Hakim, 2012].

## 2.7 Numerical weather prediction model

All forecast data used in this study origins from the numerical weather prediction (NWP) model AROME-Norway. The AROME-model is relatively new, becoming operational at Météo-France in the end of 2008 [Seity et al., 2011] and the Norwegian Meteorology Institute started using the Norwegian version AROME-Norway for their official weather forecasts at 1. October, 2013 [Norwegian Meteorological Institute, 2013].

AROME-Norway has a resolution of 2.5km with a grid size of 750x960 and 65 vertical layers [Aspelien and Køltzow, 2013], compared to the previously used HIRLAM8 and HIRLAM12 models with 8 and 12 km resolution respectively [Norwegian Meteorological Institute, 2008]. One benefit of the new model is naturally the better resolution, which among others will give large improvement for precipitation forecasts.

Forecasts are issued four times a day at: 00UTC, 06UTC, 12UTC and 18UTC, each with a 66 hour forecast horizon. These forecast are provided as point forecasts for every integer hour.

## 2.8 General statistics

### 2.8.1 Mean

For a random variable $X$, taking on values $x$, and with a probability distribution given by $f(x)$, Walpole et al. [2007] defines the expected value or mean of $X$ as

$$\mu = E(X) = \sum_x x f(x), \tag{2.39}$$

for discrete $X$, and

$$\mu = E(X) = \int_{-\infty}^{\infty} x f(x) \mathrm{d}x, \tag{2.40}$$

for continuous $X$.

Assuming a random sample $\{X_1, X_2, ..., X_n\}$ where the data in the sample are realizations of $n$ independent and identically distributed observations of the generic random variable $X$, the mean of $X$ can be estimated as

$$\hat{\mu}_X(n) \triangleq \frac{1}{n} \sum_{i=1}^{n} X_i, \tag{2.41}$$

known as the sample mean, or mean-estimator function [Stark and Woods, 2012].

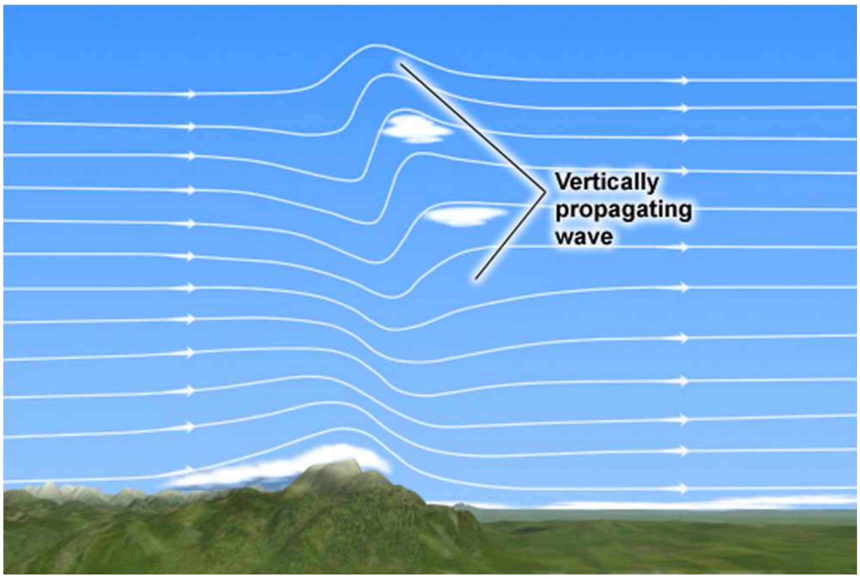

Figure 2.11: Vertically propagating mountain waves [Muller, 2014].

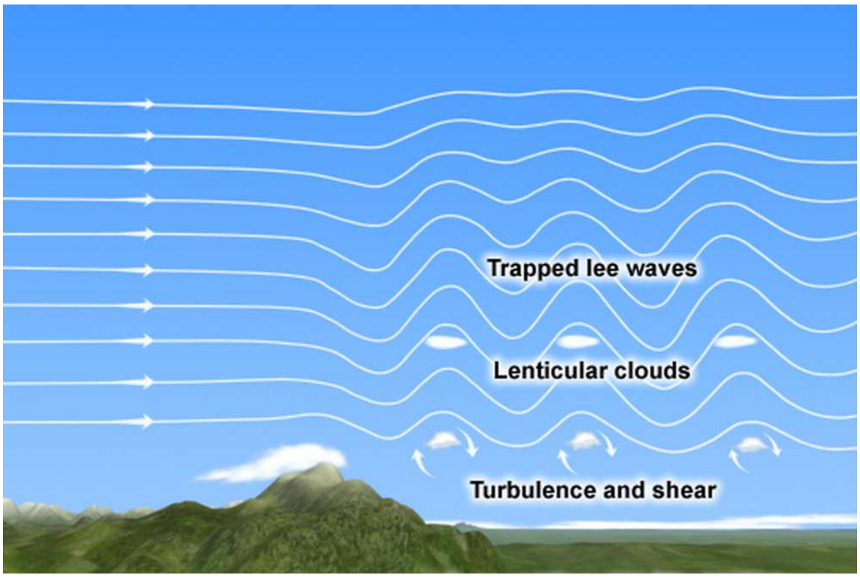

Figure 2.12: Vertically decaying mountain waves [Muller, 2014].

### 2.8.2 Variance

Walpole et al. [2007] defines the variance of a random variable $X$ with probability distribution $f(x)$ and mean $\mu$ as

$$\sigma^2 = E\left[(X-\mu)^2\right] = \sum_x (x-\mu)^2 f(x), \tag{2.42}$$

for discrete $X$, and

$$\sigma^2 = E\left[(X-\mu)^2\right] = \int_{-\infty}^{\infty} (x-\mu)^2 f(x)\mathrm{d}x, \tag{2.43}$$

for continuous $X$, where $\sigma$ is known as the standard deviation of $X$, usually abbreviated STD.

The variance-estimator function or sample variance is equivalently defined by Stark and Woods [2012] as

$$\hat{\sigma}_X^2(n) \triangleq \frac{1}{n-1}\sum_{i=1}^{n}(X_i - \hat{\mu}_X(n))^2, \tag{2.44}$$

### 2.8.3 Cumulative distribution function

For a random variable $X$, Leon-Garcia [1994] defines the cumulative distribution function (cdf) as

$$F_X(x) = P(X \leq x) \quad \text{for} \quad -\infty < x < \infty, \tag{2.45}$$

which means the probability of a random variable $X$ taking on a value in the set $(-\infty, x]$. The cdf has the following properties:

1. $0 \leq F_X(x) \leq 1$,
2. $\lim\limits_{x\to\infty} F_X(x) = 1$,
3. $\lim\limits_{x\to-\infty} F_X(x) = 0$,
4. $F_X(x)$ is a nondecreasing function of $x$, which means if $a < b$ then, $F_X(a) \leq F_X(b)$,
5. $F_X(x)$ is continuous from the right, which means for $h > 0$, $F_X(b) = \lim\limits_{x\to\infty} F_X(b+h) = F_X(b^+)$.

### 2.8.4 Probability density function

Leon-Garcia [1994] defines the probability density function of a random variable $X$, if it exists, as

$$f_X(x) = \frac{\mathrm{d}F_X(x)}{\mathrm{d}x}, \tag{2.46}$$

with the following properties:

1. $f_X(x) \geq 0$.
2. $P(a \geq X \geq b) = \int_a^b f_X(x)\mathrm{d}x$.
3. $F_X(x) = \int_{-\infty}^{x} f_X(t)\mathrm{d}t$.
4. $\int_{-\infty}^{\infty} f_X(t)\mathrm{d}t = 1$.

### 2.8.5 Median

For a distribution of a random variable $X$, the median of the distribution is given by Hogg and Craig [1978] as the value of $x$ fulfilling the following two conditions

$$P(X < x) \leq \frac{1}{2}, \tag{2.47}$$

$$P(X \leq x) \geq \frac{1}{2}. \tag{2.48}$$

### 2.8.6 Error measures

A standardization of the performance evaluation of short-term wind power prediction models are given by Madsen et al. [2005]. Here the prediction error is defined as the difference between measured and predicted value

$$e(t+k|t) = P(t+k) - \hat{P}(t+k|t), \tag{2.49}$$

where $t+k$ is the lead time (usually in hours) and $P$ and $\hat{P}$ are the true and predicted power respectively. Dividing the prediction error $e$ on the installed capacity $P_{inst}$ will give the normalized prediction error,

$$\epsilon(t+k|t) = \frac{1}{P_{inst}} \left( P(t+k) - \hat{P}(t+k|t) \right). \tag{2.50}$$

The prediction error can be decomposed into a systematic error $\mu_e$ and a random error $\chi_e$ so that

$$e = \mu_e + \chi_e, \tag{2.51}$$

where $\mu_e$ is a constant and $\chi_e$ is a zero mean random variable.

### Normalized root mean square error

The Root Mean Square Error (RMSE) and the Normalized Root Mean Square Error(NRMSE) can be defined as

$$RMSE(k) = \left( \frac{1}{N} \sum_{t=1}^{N} e^2(t+k|t) \right)^{\frac{1}{2}}, \tag{2.52}$$

and

$$NRMSE(k) = \left( \frac{1}{N} \sum_{t=1}^{N} \epsilon^2(t+k|t) \right)^{\frac{1}{2}}, \tag{2.53}$$

where $N$ is the number of predictions made in the time period evaluated. These error measures includes contributions from both the systematic and random error [Madsen et al., 2005].

### Model comparison

In order to evaluate and quantify the benefit of using a new model compared to a reference model, a improvement parameter $I$ can be used, which for a given lead time is defined as [Madsen et al., 2005]

$$I_{ref,EC} = 100 \cdot \frac{EC_{ref}(k) - EC(k)}{EC_{ref}(k)} (\%), \tag{2.54}$$

where $EC$ stands for Evaluation Criterion, for instance the RMSE or NRMSE, of the new model and the reference model.

## 2.8.7 Directional statistics

When dealing with directional wind data measurements problems will be encountered using common statistical features such as mean and variance. Reason for this being that these features are based upon linear statistics, thus a new set of statistical features for the non-linear case must be obtained. For instance, taking the mean of two angles such as $355\,^\circ$ and $5\,^\circ$ using linear statistics would result in $180\,^\circ$, i.e. south. However, a more suitable mean when dealing with wind directions would be $0\,^\circ$, i.e. north which is the complete opposite.

### Directional mean

Jammalamadaka and Sengupta [2001] describes the following method for finding the directional mean of a dataset $D = \{\theta_1, \theta_2, ..., \theta_n\}$, consisting of angles $\theta$ measured in radians.

First convert the data into two-dimensional unit vectors $\boldsymbol{r}_1, ...\boldsymbol{r}_n$ which can be represented on a unit circle so that $\|\boldsymbol{r}_i\| = 1$ for $i = 1, ..., n$, as

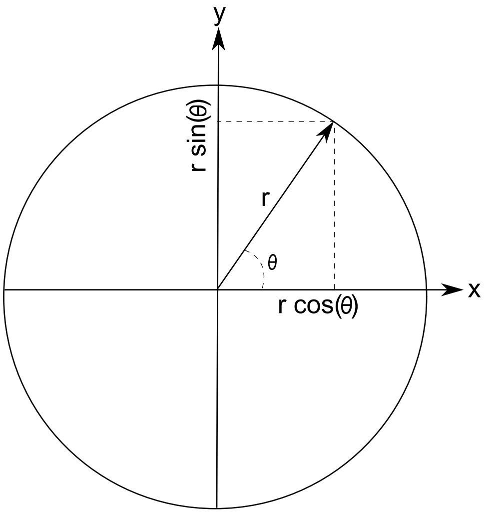

Figure 2.13: Relation between kartesian and polar coordinates [Jammalamadaka and Sengupta, 2001].

seen in Figure 2.13 and with the relation between the kartesian and polar coordinates given by

$$\boldsymbol{r} = (x, y) = (r\cos\theta, r\sin\theta)\,. \tag{2.55}$$

A resultant vector $\boldsymbol{R}$ can then be found by summing the $n$ unit vectors

$$\boldsymbol{R} = \left(\sum_{i=1}^{n}\cos\theta_i, \sum_{i=1}^{n}\sin\theta_i\right) = (C, S), \tag{2.56}$$

where $\|\boldsymbol{R}\| = \sqrt{C^2+S^2}$ is the length $R$.

The directional mean can then be found with solutions specified for each quadrant of the unit-circle as [Jammalamadaka and Sengupta, 2001]

$$\bar{\theta} = \arctan\left(\frac{S}{C}\right) = \begin{cases} \arctan\left(\frac{S}{C}\right), & \text{for} \quad C > 0, \quad S \geq 0, \\ \frac{\pi}{2}, & \text{for} \quad C = 0, \quad S > 0, \\ \arctan\left(\frac{S}{C}\right) + \pi, & \text{for} \quad C < 0, \\ \arctan\left(\frac{S}{C}\right) + 2\pi, & \text{for} \quad C \geq 0, \quad S < 0, \\ \text{undefined}, & \text{for} \quad C = 0, \quad S = 0. \end{cases} \tag{2.57}$$

### Directional variance

It is often usefull to find a measure for how widely spread the dataset are. For this purpose Mahan [1991] uses the length $R$ of the resultant vector $\boldsymbol{R}$. A large $R$ indicates concentrated data, while a small $R$ indicates that the data are widely spread, as the data points in many different directions. In

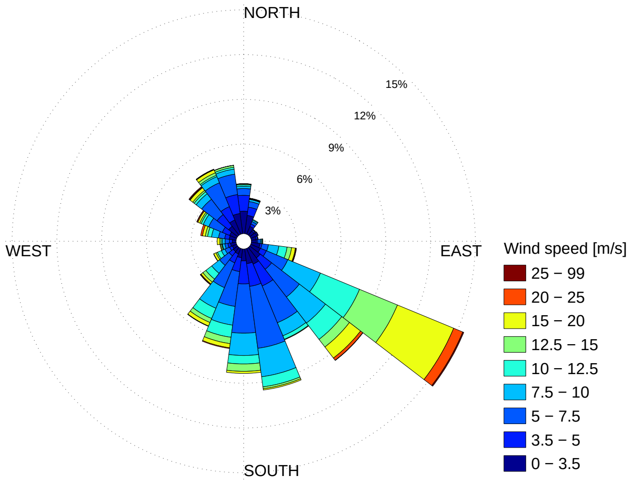

Figure 2.14: Example of a wind rose

the case of equally dispersed data, $R = 0$, and no mean can be obtained. As a result $1 - R$ becomes a measure of the dispersion of the data and the circular variance becomes

$$\sigma^2 = 2(1 - R), \tag{2.58}$$

where $\sigma$ is known as the circular standard deviation, an equivalent to the linear standard deviation described in Section 2.8.2 [Mahan, 1991].

### Circular histogram

A circular histogram, or rose diagram, is basically a histogram where the bars are replaced by sectors around a circle. Each bar is divided into bins representing data intervals, with the radius of each bar representing the percentage of the total data observed within a given sector. The angular width of the bars are constant [Mardia and Jupp, 2000].

Rose diagram representation of wind direction and speed are known as wind roses. An example of a wind rose can be seen in Figure 2.14. The circle is divided into 24 directional sectors, each representing 15° and each sector are further divided into bins representing different wind speed intervals. The radius of each sector now represents the percentage number of wind speed measurements observed for the given sector.

## 2.9 Markov chains

The theory of Markov chains was according to Balzter [2000] developed by the Russian mathematician Andrei Andreyevich Markov (1856-1922) in his paper *Extension of the Limit Theorems of Probability Theory of a Sum of Variables Connected in a Chain* [Markov, 1907].

Balzter [2000] defines a Markov chain as a stochastic process fulfilling the Markov property with a discrete state space and a discrete or continuous parameter space. A stochastic process is a collection of random variables such that for each index $t \epsilon T$,the index set, $X(t)$ is a random variable [Ross, 2010]. Usually, $t$ is interpreted as time, making $X(t)$ the state of the process at time $t$.

For a first-order Markov chain, the Markov property states that the next state only depends on the present state, which for a discrete case is given as [Ross, 2010]

$$P_{ij} = P(X_{t+1} = j | X_t = i, ..., X_0 = i_0) = P(X_{t+1} = j | X_t = i), \qquad (2.59)$$

for all $t \geq 0$ and states $i_0, ..., i_{t-1}, i, j$, where $X_0$ denotes the initial state of the process and $X_t = i$ that the process is in state $i$ at time $t$. $P_{ij}$ is the probability of going from state $i$ to state $j$, or the transition probability, and is independent of $t$. For a second order Markov chain the process depends on the current state and the immediately preceding state, following the same pattern for higher orders [Shamshad et al., 2005].

Combining all the transition probabilities between $k$ states, a transition matrix $\boldsymbol{P}$ of a first-order Markov chain can be defined as [Balzter, 2000]

$$\boldsymbol{P} = \begin{bmatrix} p_{1,1} & p_{1,2} & \cdots & p_{1,k} \\ p_{2,1} & p_{2,2} & \cdots & p_{2,k} \\ \vdots & \vdots & \ddots & \vdots \\ p_{k,1} & p_{k,2} & \cdots & p_{k,k} \end{bmatrix}, \qquad (2.60)$$

where $p_{1,2}$ is the probability of going from state 1 to state 2. The following conditions must be fulfilled:

1. $p_{ij} \geq 0, \forall\, i, j \geq 1$,

2. $\sum_{j=1}^{k} p_{ij} = 1$.

The first condition simply says that all the probabilities must be positive, while the second condition states that the probability of going from one state to any other possible state must be equal 1. If it does not equal 1, it means that all the states are not identified in the transition matrix.

For a second-order Markov chain, the transition matrix becomes [Shamshad et al., 2005]

$$\boldsymbol{P} = \begin{bmatrix} p_{1,1,1} & p_{1,1,2} & \cdots & p_{1,1,k} \\ p_{1,2,1} & p_{1,2,2} & \cdots & p_{1,2,k} \\ \vdots & \vdots & \ddots & \vdots \\ p_{1,k,1} & p_{1,k,2} & \cdots & p_{1,k,k} \\ p_{2,1,1} & p_{2,1,2} & \cdots & p_{2,1,k} \\ p_{2,2,1} & p_{2,2,2} & \cdots & p_{2,2,k} \\ \vdots & \vdots & \ddots & \vdots \\ p_{k,k,1} & p_{k,k,2} & \cdots & p_{k,k,k} \end{bmatrix}, \tag{2.61}$$

where $p_{ijl}$ is the transition probability of going to state $l$, given that the current state is $j$ and the previous state was $i$. The same conditions must be fulfilled:

1. $p_{ijl} \geq 0$, $\forall\ i, j, l \geq 1$,
2. $\sum_{l=1}^{k} p_{ijl} = 1$.

It is possible to estimate the transition probabilities of a first- and second-order Markov chain, using Maximum Likelihood, as [Carpinone et al., 2010]

$$p_{ij} = \frac{n_{ij}}{\sum_{j=1}^{k} n_{ij}}, \tag{2.62}$$

and

$$p_{ijl} = \frac{n_{ijl}}{\sum_{l=1}^{k} n_{ijl}}, \tag{2.63}$$

respectively, where $n$ is the number of occurrences for a given state.

If $p_{ij} = 1$, the state $i$ is said to be an absorbing state, which means that if the process enters this state, it cannot leave it [Balzter, 2000]. A state is either [Ross, 2010]:

- Recurrent: If the process is in state $i$, the probability of returning to this state is 1,
- Transient: If the process is in state $i$, the probability of returning to this state is less than 1.

Further the Markov chain is said to be irreducible if it all states communicate, i. e. accessible to each other.

By the Chapman-Kolmogorov equations, the probability of going from state $i$ to state $j$ in $t$ steps, known as the $t$-step transition probability is defined as [Ross, 2010]

$$p_{ij}^{t} = P(X_{t+k} = j | X_k = i), \quad \forall t, k \geq 0, \quad i, j \geq 0 \tag{2.64}$$

and

$$p_{ij}^{t+m} = \sum_{k=0}^{\infty} o_{ik}^{t} o_{kj}^{m}, \quad \forall t, m \geq 0, \quad \forall i, j, \tag{2.65}$$

where $p_{ij}^{t+m}$ is the $t + m$ step transition probability of going from state $i$ to state $j$. This can also be expressed using matrices so that

$$\boldsymbol{P^{(t+m)}} = \boldsymbol{P^{(t)}} \boldsymbol{P^{m}}, \tag{2.66}$$

where $\boldsymbol{P^{(t)}}$ is the $t$-step transition matrix.

# Chapter 3

# Methods

## 3.1 Site and time

Fakken wind farm is located at Vannøya in Troms county in Northern Norway. A map of the area is given in Figure 3.1. The wind farm consist of 18 Vestas V90 3.0MW horizontal axis wind turbines [Troms Kraft AS, 2012] with hub height of 80 meter and a rotor diameter of 90 meter with three turbine blades [Vestas Wind Systems A/S, 2013]. All the turbines are sited on the southwestern tip of Vannøya, with a mountain range located to the west, going across the island from south to north. Surrounding Vannøya are several other mountainous islands and fjords, resulting in a complex wind regime. Both local and regional mountain waves are expected at the site. The local mountain waves as a result of the local mountain regions on the islands itself, and the regional as an effect of the great mountain range between Norway and Sweden to the southwest.

Three sets of wind data have been provided and used in this study,

1. In-situ measurements from meteorological station located at Fakken wind farm (courtesy of Troms Kraft AS),

2. In-situ measurements from a reference wind turbine, WTG08, at Fakken wind farm (courtesy of Troms Kraft AS),

3. Numerical weather prediction data obtained by the AROME-Norway model for the Fakken wind farm area (courtesy of the Norwegian Meteorological Institute),

with coordinates for the site, meteorology station and WTG08 given in Table 3.1. In-situ measurements are given for the time period 1. May 2013 to 1. May 2014, while the AROME-Norway forecasts are given for the time period between 2. May 2013 and 31. March 2014.

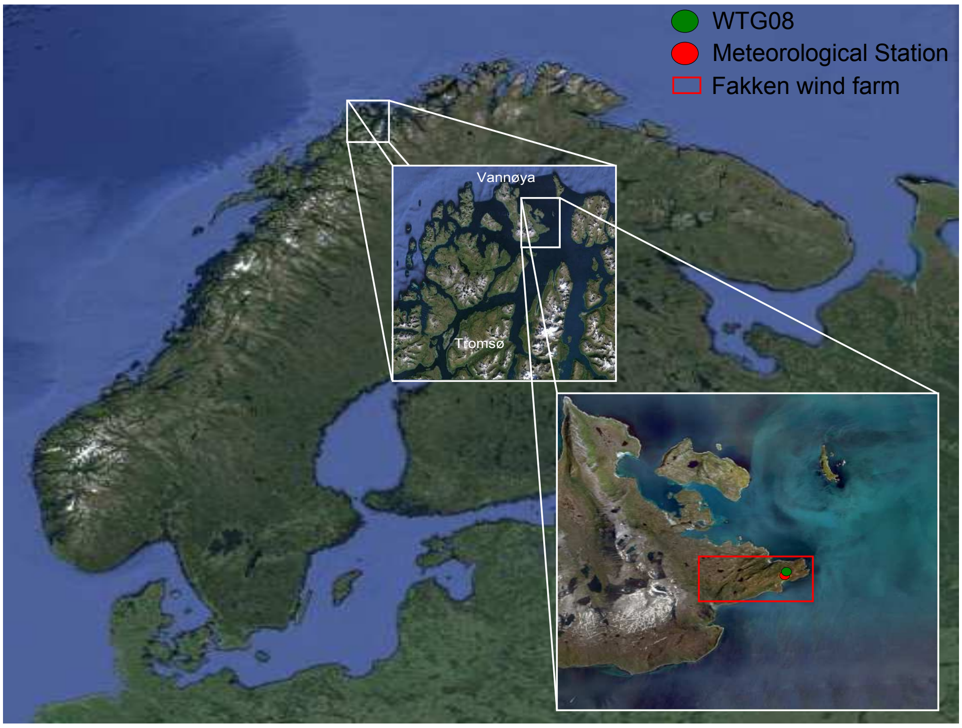

Figure 3.1: Map of the location and surrounding area of Fakken wind farm with WTG08 and meteorology pointed out.

| Euroref 89 | UTM-zone 33 | |
|---|---|---|
| **Fakken windfarm** | | |
| Coordinates | 65660E | 710680E |
| | 7828400N | 7768400N |
| **Met. station** | | |
| Coordinates | 693269.567E | 7785030.852N |
| Kote | 68 | |
| Height [m] | 80 | |
| **WTG08** | | |
| Coordinates | 693339.50E | 7785249.78N |
| Kote | 66.13 | |
| Hub height [m] | 80 | |

Table 3.1: Site coordinates

## 3.2 Data collection

### 3.2.1 In-situ measurements from VestasMetPanel 3000

The meteorological station VestasMetPanel 3000 measures the wind speed and wind direction at 45 and 80 meter heights. From these measurements the following data are available,

- 10-minute minimum value
- 10-minute average value
- 10-minute maximum value
- 10-minute variance

for both the speed and direction parameters [Vestas Wind Systems A/S, 2008]. Each record is time-stamped at the start of each record, i.e. data recorded from 13:30:00 to 13:40:00 will be time-stamped 13:30:00, but stored at 13:40:00.

#### Anemometer

Wind speed measurements at the meteorological station are performed using two WAA151 anemometers, installed at the respective heights. An image of these wind anemometers are seen in Figure 3.2 with the cup wheel assemble, sensor shaft and lower body pointed out.

As described by Vaisala Oyj [2002a] the anemometer WAA151 is an optoelectronic, fast-response and low threshold anemometer. The wind speed is measured by three light-weight conical cups which are attached to the cup wheel. According to the producer, this will provide excellent linearity for the entire operating range, which goes up to 75 m/s. Attached to the cup wheel's shaft is a chopper disc and as the wind rotates the cup wheel, this chopper disc will cut an infrared light beam 14 times per revolution. This generates a pulse train output from a phototransistor.

The output pulse rate makes it possible to determine the wind speed as they can be regarded as directly proportional, for instance 246 Hz = 24.6 m/s. However, in order to increase the accuracy of the measurements the characteristic transfer function is advised to be used as noted in Table 3.2.

To avoid problems related to freezing in cold climates, a heating element of usually 10 W is installed in the shaft tunnel to keep the temperature of the bearings above freezing levels. Key technical specifications are shown in Table 3.2.

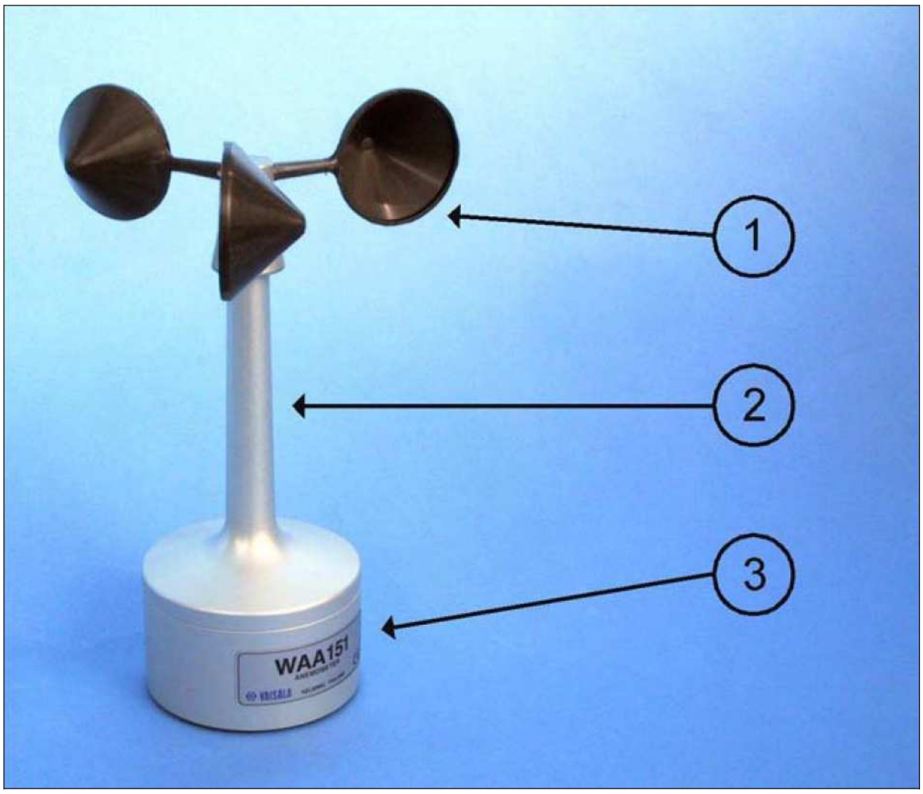

Figure 3.2: WAA151 anemometer, where (1) is the cup wheel assembly, (2) the sensor shaft and (3) the lower body [Vaisala Oyj, 2002a].

| **Property** | **Description/Value** |
|---|---|
| Measuring range | 0.4 - 75 m/s |
| Starting threshold | $< 0.5$ m/s $^{1)}$ |
| Accuracy (within 0.4 to 60 m/s): | |
| With Characteristic Transfer function | ± 0.17 m/s $^{2)}$ |
| With "simple transfer function" $U_f = 0.1xR$ | ± 0.5 m/s |
| Dimensions | 240 (h) x 90 (Ø) mm |
| Weight | 570g |

$^{1)}$Measured with cup wheel in position least favored by flow direction. Optimum position yields $< 0.35$ m/s starting threshold.
$^{2)}$Standard Deviation

Table 3.2: Key technical specifications for WAA151 Anemometer [Vaisala Oyj, 2002a].

### Wind Vane

In addition to the two anemometers, two WAV151 wind vanes are installed at the same heights on the meteorology station. These are used to measure the wind direction. The WAV151 wind vane is a counter balanced, low threshold optoelectronic wind vane [Vaisala Oyj, 2002b]. Figure 3.3 shows the WAV151 wind vane with the vane assembly, sensor shaft and lower body pointed out.

Wind direction are measured using infrared LEDs and phototransistors which are mounted on six orbits on each side of a 6-bit GRAY-coded disc [Vaisala Oyj, 2002b]. As the wind direction changes, the vane is rotated causing the disc to create changes in the code received by the phototransistors. In order to eliminate ambiguities, the code is changed in steps of 5.6 °, one bit at a time.

A 10 W heating element is installed in the shaft tunnel to avoid the temperatures of the bearings to reach freezing levels. Key technical specifications are shown in Table 3.3.

## 3.2.2 In-situ measurements from WTG08

For the WTG08 wind turbine, following measurements of the wind speed and power have been provided

- 10-minute minimum value
- 10-minute average value
- 10-minute maximum value
- 10-minute variance

in addition to

- 10-minute average value of the temperature
- 10-minute absolute average value of the direction.

These date are collected by equivalent measurement instruments as described for the VestasMetPanel 3000.

## 3.2.3 Numerical weather prediction data

Hourly point prediction data are obtained from the numerical weather prediction (NWP) model AROME-Norway. Forecasts issued at 00 UTC-time are provided, with a forecast horizon of 24 hours. These data includes prediction of the wind speed and wind direction of Fakken wind farm for two layers, L64 and L65.

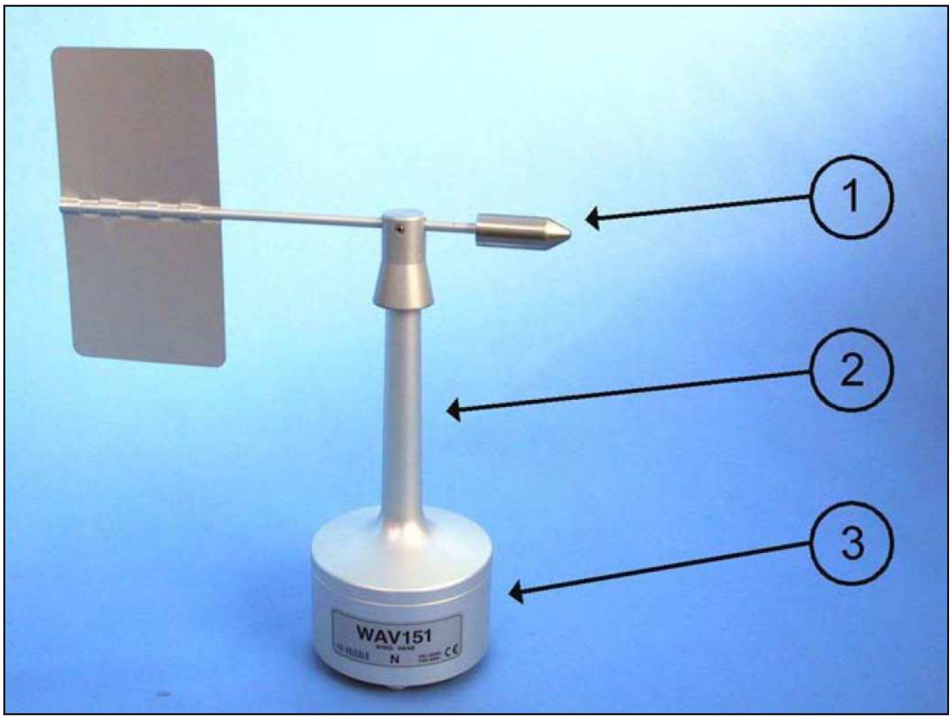

Figure 3.3: WAV151 wind vane, where (1) is the vane assembly, (2) the sensor shaft and (3) the lower body [Vaisala Oyj, 2002b].

| **Property** | **Description/Value** |
|---|---|
| Sensor/Transducer type | Vane/Optical code disc |
| Measuring range | 0 - 360 ° |
| Starting threshold | < 0.4 m/s |
| Accuracy | Better than ±3 ° |
| Dimensions | 300(h) x 90(Ø) mm |
| | Swept radius of vane: 172 mm |
| Weight | 660g |

Table 3.3: Key technical specifications for WAV151 Wind Vane [Vaisala Oyj, 2002b].

Height of each layer varies with the weather but in the general the L64 layer is approximately 34 meters above the ground, while the L65 layer is approximately 10 meters above ground. For Fakken wind farm, the model height is approximately 20 meters above sea level, but in reality the wind farm lies 57 meter above sea level. The L64 and L65 layers are therefore in practice at 54 and 30 meters above sea level respectively, and this must be taken into account when extrapolating to hub height.

Rewriting the power law given by Equation 2.7 in Section 2.3.2, it is possible to derive an expression for the Hellman constant $a$ as follows

$$\begin{aligned}
u(z) &= u(z_r)\left(\frac{z}{z_r}\right)^a \\
\Rightarrow &\frac{u(z)}{u(z_r)} = \left(\frac{z}{z_r}\right)^a \\
\Rightarrow &\ln\left(\frac{u(z)}{u(z_r)}\right) = a\ln\left(\frac{z}{z_r}\right), \\
\Rightarrow &a = \frac{\ln\left(\frac{u(z)}{u(z_r)}\right)}{\ln\left(\frac{z}{z_r}\right)} \\
a &= \frac{\ln(u(z)) - \ln(u(z_r))}{\ln(z) - \ln(z_r)}
\end{aligned} \tag{3.1}$$

where $a$ now can be estimated as the average of the measurements from the two heights on the meteorological station or by using the predictions from the L64 and L65 layers, expressed mathematically as

$$\hat{a}_{met.station} = \frac{1}{n}\sum_{i=1}^{n}\left(\frac{\ln(u(z_{80,i})) - \ln(u(z_{45,i}))}{\ln(z_{80}) - \ln(z_{45})}\right), \tag{3.2}$$

and

$$\hat{a}_{forecast} = \frac{1}{n}\sum_{i=1}^{n}\left(\frac{\ln(u(z_{L64,i})) - \ln(u(z_{L65,i}))}{\ln(z_{L64}) - \ln(z_{L65})}\right), \tag{3.3}$$

respectively. Here $n$ is the total number of data points, i. e. measurements or forecasts, and $u(z_{80,i})$ is the $i$'th measurement of the wind speed at 80 meters height, equivalently $u(z_{L64})$ is the $i$'th wind speed forecast at 34 meters height.

Using the estimated Hellman exponent the two forecast layers L64 and L65 can be extrapolated to hub height using the power law, with $z = 117$m and $z_r = 34$m for the L64 layer and $z = 117$m and $z_r = 10$m for the L65 layer. The $z$ height is calculated as follows

$$\begin{aligned}
z =& h_{WTG08} + h_{Fakken} - h_{model} \\
=& 80m + 57m - 20m \\
=& \underline{117m}
\end{aligned}, \tag{3.4}$$

where $h_{WTG08}$ is the hub height of WTG08, $h_{Fakken}$ the approixmately height of Fakken wind farm above sea level and $h_{model}$ the height of the AROME-Norway model for Fakken wind farm.

At the initiating of each forecast, the first hours will be influenced by some noise and the longer forecast horizon the more uncertain the forecast will be.

## 3.3 Power prediction models

### 3.3.1 Notation

The following notations will be used when dealing with the power prediction models.

$P$: Measured power from WTG08 [kW]

$\hat{P}$: Power forecast [kW]

$U$: Measured wind speed from meteorological station[m/s]

$\hat{U}$: Wind speed forecast using NWP [m/s]

$D$: Measured wind direction from meteorological station [deg]

$\hat{D}$: Wind direction forecast using NWP [deg]

$t_0$: Current time [hrs]

$t_m$: $m$ = -1, 1, 2, time at -1, 1 and 2 hours from current time.

### 3.3.2 Persistent model

The persistent model is often used as a reference model for evaluating short-term power prediction models. It is given by Carpinone et al. [2010] as

$$\hat{P}(t_{h+m}|t_h) = P(t_h), \tag{3.5}$$

for $m = 1, 2, 3, ...$ and where $\hat{P}(t_{h+m}|t_h)$ is the power forecast for time $t_{h+m}$ made at time $t_h$ and $P(t_h)$ is the measured power at time $t_h$. So in words this model simply states that future power production will equal the last measured power. However, even though it is a simple predictor, it will perform rather well for the first look-ahead times due to the atmospheric changes occurring relatively slow [Madsen et al., 2005].

### 3.3.3 Training and test data

In order to find out how well a prediction model perform, it should be tested on new and independent test data [Madsen et al., 2005]. The available data should therefore be divided into two parts, a training period, and a test period, of which the prediction model is trained using the training data before the capability of the model is tested using new and independent data from the test period.

This method will not only be a more correct way of finding the performance, but it will also easily show cases of over-training. If the models complexity increases, it will become more capable of distinguishing between the input data, leading to good performance when the model is tested on the same data it was trained with. However, such a model will perform poorly when tested on new independent data, as it is over-trained [Madsen et al., 2005].

In this study, the leave one out method will be used to provide both training data and new, independent test data. Each test period will consist of a month of data, with the remaining 10 month being training data. Error measures will only be based on the test period.

### 3.3.4 Markov chain model

An overview of the algorithm for the Markov chain model are shown in Figure 3.4. All the 10-minute averaged data are loaded from xlsx-format into Matlab with an array for each of the various input data, such as measured wind speed, power output and so on.

In the next step the 10-minute average data are converted to hourly data. The measured power output are converted as hourly arithmetic averages, while for measured wind speed and direction the last 10-minute average of every hour were chosen, as they are closest to the point predictions provided by the NWP. This means that the data measured between 10:50 and 11:00, timestamped as 10:50, was used as the hourly data value for 11:00. At the same time, all the measured data and forecast data are made sure to have the same relative time, which was chosen to be UTC-time.

Further all missing dates and NaN-values (no available measurements) are removed from all the arrays so that each array consist of the same amount of data for the same time. Negative values are set equal to 0 and power values above rated power are set to rated power. This is mainly done to simplify the definition of the states later on. All forecast data are extrapolated to hub height using the power law and the estimated Hellman constant $a$ using the average between Equation 3.2 and Equation 3.3.

For each of the three input types, power P [kW], wind speed U [m/s] and wind direction D [deg], number and spacing of state intervals are chosen. These have currently been chosen to be

- P: 20 states, of which 19 are equally spaced between 0 and 3000 kW, with an additional cut-off states being defined when wind speeds are above 10 m/s and power output equals zero,

- U: 9 states, of which 0 - 3.5 m/s (cut-inn speed) is the first state, the next 7 states are between 3.5, 5, 7.5, 10,..., 15, 20, 25 and the last state being all wind speed above cut-off speed. Note that two states are given between the rated wind speed at 15 m/s and the cut-off speed at 25 m/s,

- D: 8 equally spaced states representing the cardinal directions north, east, south, west and the intercardinal directions northeast, southeast, southwest and northwest. Each direction covers 45°, with 22.5° on each side of the directional centers. (These directions can be seen in Figure 4.3 in Chapter 4).

For every data array, each element of the vector is converted to its corresponding state value, for instance a wind speed value of 0 m/s would be denoted as state 1, while a wind speed value of 30 m/s denoted as state 9 (as this is the total number of states for wind speeds). This is done due to practical reasons in the algorithm, making it both more computational effective and easier to handle several input parameters to the model later on.

The arrays, now with each element representing the state according to their corresponding parameter state interval, are then divided into test and train periods. For each of the 11 months, 11 test arrays are made containing data for a whole month, with corresponding 11 arrays consisting of data from the remaining 10 months, to be used as a training data for making the transition matrix.

For each Markov chain model, a set of parameters must be defined as input to the model. This could for instance be current measured wind speed ($U(t_0)$)and 2-hour point forecast of the wind speed ($\hat{U}(t_2)$) or any other combination from the available data. It is possible to also define the output state parameters, however this is set to be the power prediction with a 2-hour prediction horizon by default, i. e. a forecast of the average power output between the next hour ,$t_1$, and two hours into the future, $t_2$.

Now that all the prerequisite are taken care of, the actual power prediction can be made. Starting by the first test month, a transition matrix is made using data from the remaining training data. With the example above, using as input parameters the current measured wind speed and the 2-hour point forecast and the predicted power output in 2-hours, the transition matrix $\boldsymbol{P}$ would look become

$$\boldsymbol{P} = \begin{bmatrix} p_{1,1,1} & p_{1,1,2} & \cdots & p_{1,1,\hat{p}} \\ p_{1,2,1} & p_{1,2,2} & \cdots & p_{1,2,\hat{p}} \\ \vdots & \vdots & \ddots & \vdots \\ p_{1,\hat{u},1} & p_{1,\hat{u},2} & \cdots & p_{1,\hat{u},\hat{p}} \\ p_{2,1,1} & p_{2,1,2} & \cdots & p_{2,1,\hat{p}} \\ p_{2,2,1} & p_{2,2,2} & \cdots & p_{2,2,\hat{p}} \\ \vdots & \vdots & \ddots & \vdots \\ p_{u,\hat{u},1} & p_{u,\hat{u},2} & \cdots & p_{u,\hat{u},\hat{p}} \end{bmatrix}, \tag{3.6}$$

where $p_{ijl}$ indicates the probability of going to the power output state $l$, given that the current measured wind speed is in state $i$ and the 2-hour point forecast in state $j$. Using the default number of states defined above, the dimension of the matrix would be 81x20, i. e. number of wind speed states to the second power times the number of power output states.

For the test month, the current state of the first element of the input parameter arrays are found. These values indicates a given row in the transition matrix, which can be used to find the probabilistic forecast of the power output, i. e. the column elements of that particular row. Currently the model give as output the most probable power state, which again can be converted back to a specific power value by using the definition of the power states. In the case that no previous observations have been recorded for a specific event, i. e. the row in the transition matrix consists only of 0's, 0 power output will be used as the forecast.

This procedure is done for every hourly data point in the test month, repeated for a new test month and new training months until all the data have been used for testing and training. This results in a complete set of independently tested data. The NRMSE are calculated both monthly and for the whole period.

### 3.3.5 Combined Markov chain and persistent model

The combined Markov chain and persistent model use the MC model by default, but in the case of no previously recorded data for a given row in the transition matrix, the persistent model with $m = 2$ is used instead. This means that instead of choosing the 0 power output prediction the average power output for the last hour will be used instead.

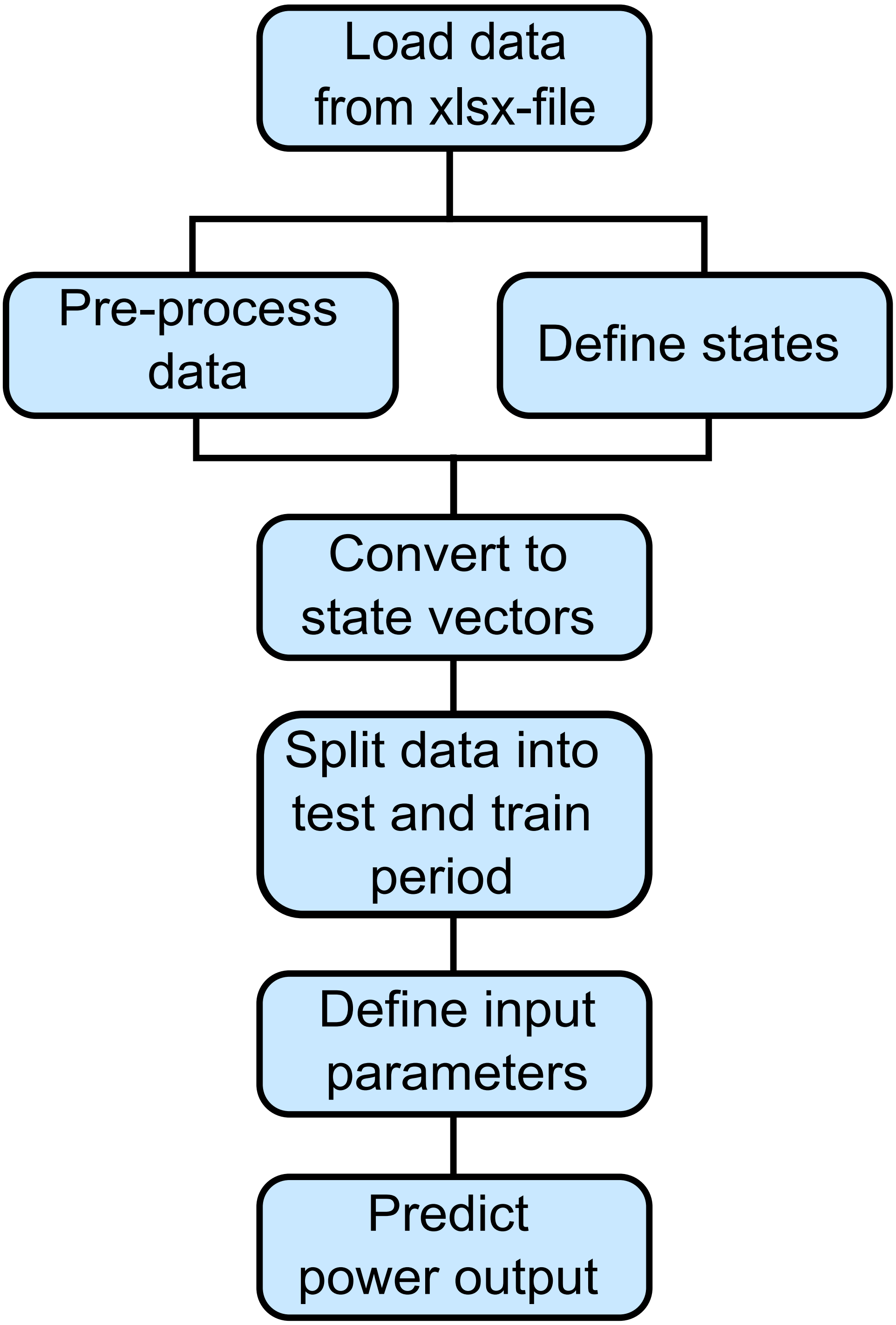

Figure 3.4: Algorithmic overview of the Markov chain wind power prediction model.

# Chapter 4

# Results

Using Equation 3.2 and Equation 3.3 the Hellman constant was estimated to be $\hat{a}_{met.station} = 0.11$ and $\hat{a}_{forecast} = 0.09$ and therefore a Hellman constant of $a = 0.10$ was chosen for extrapolation of forecast data from the layer height to hub height. Such low values of $a$ implies a rather smooth surface. In this case the solution of the power law (Equation 2.7) will go towards the solution of the logarithmic law (Equation 2.3) [Emeis, 2013]. The power law was therefore chosen for the extrapolation process, due to its mathematical simplicity. As the extrapolation of the two layers L64 and L65 was found to be relatively equal, only extrapolated values for the L64 layer will be used in the proceedings. All in-situ measurements used are from 80 meter height.

As wind forecasts are only available in the time period 2. May 2013 to 31. March 2014, the same time period is used for the in-situ measurements from Fakken in the following sections. This is to ensure the same amount of data from the same time period, to be able to directly compare measured and forecast data in the proceeding sections. An exception is Section 4.3 were only the in-situ measurements are used in the analysis. In this section the time period 1. May 2013 to 31. April 2014 are used instead.

## 4.1 Rose diagrams

The wind distribution as a function of direction for measurements from the meteorology station at Fakken are given in Figure 4.1, and for the weather forecast in Figure 4.2.

Starting with Figure 4.1, the most common wind directions seen are between southeast and southwest and from the north-northwest, with southeast being the most dominant direction. Winds from the southeast have a higher occurrence of high wind speeds compared to the other directions. For the other directions the wind distribution between each sector are quite similar.

Looking at the rose diagram of the wind forecast (Figure 4.2) some drastic changes can be observed. Still the most dominant wind direction is from southeast, with most of the predicted winds from between a southeasterly and a southwesterly direction. However the winds are now more evenly spread within these sectors and not decreasing from southeast to southwest as was the case of the real measurements. In addition the high wind speeds seen from the southeast above 12.5 m/s are either not present or drastically reduced between the two rose diagrams. Further the northwesterly winds seen in Figure 4.1 are now seen as northern winds.

Figure 4.3 shows a map of the surrounding areas of Fakken wind farm (red rectangle) with the wind directions displayed on a circle around the map. Comparing with the wind directions seen in Figure 4.1 it is possible to observe that the dominant winds from the southeast corresponds with the strait between Arnøya and Lenangsøyra. Further the southern winds corresponds to the strait between Reinøya and Lenangsøyra, while the southwestern directions points to the straits and area between Vannøya, Ringvassøya and Reinøya. Winds blowing from the north-northwest are winds coming in from the ocean, following the curvature of the mountain range on Vannøya. Arnøya covers almost the entire eastern direction while the mountain range at Vannøya covers both the western and part of the southwestern and northwestern directions.

Comparing with Figure 4.2 the weather forecast predicts more winds blowing in from the open ocean to the north, lower occurrence of winds from the strait between Arnøya and Lenangsøyra and instead more winds blowing from direction of Lenangsøyra, Reinøya and Ringvassøya.

### 4.1.1 Case study

Figure 4.4 and Figure 4.5 shows a case study of 27. October 2013 for measurements from the meteorology station and weather forecasts respectively.

In the first figure the winds throughout the day are mainly blowing from a southeastern direction with most wind intensities being in the range 5 - 15 m/s and some in the range 15-20 m/s. The second figure have much lower wind intensities with most being in the range 0 - 12.5 m/s. Still the dominant wind direction is to the southeast, but a higher number of predicted winds are also seen to the east.

## 4.2 Power curve

Power curves for the WTG08 are shown in Figure 4.6 and Figure 4.7. The former shows the power output of WTG08 as a function of measured wind speeds (blue circles), while the latter as a function of forecast wind speed (red circles). In both figures the theoretical power curve is given in black with the cut-in, rated and cut-off wind speeds shown as lines at 3.5 m/s, 15 m/s and 25 m/s respectively.

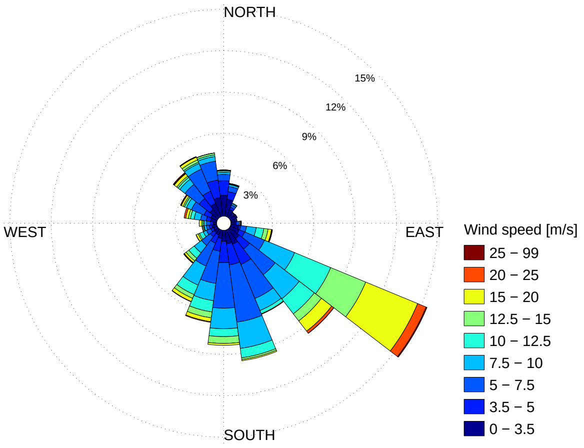

Figure 4.1: Rose diagram of in-situ measurements from the meteorology station at Fakken wind farm, in the period 2. May 2013 - 31. March 2014 (UTC-time).

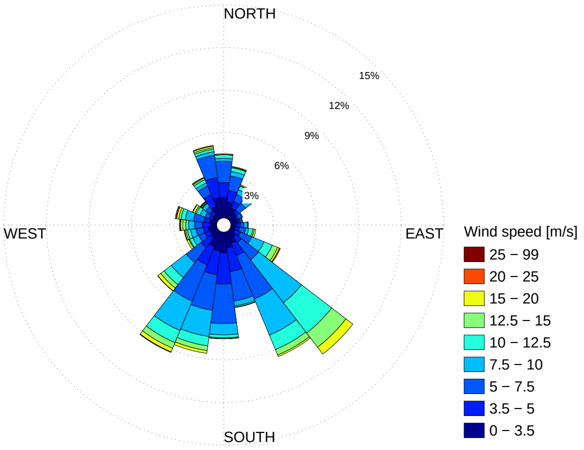

Figure 4.2: Rose diagram of the forecast wind at Fakken wind farm, in the period 2. May 2013 - 31. March 2014 (UTC-time).

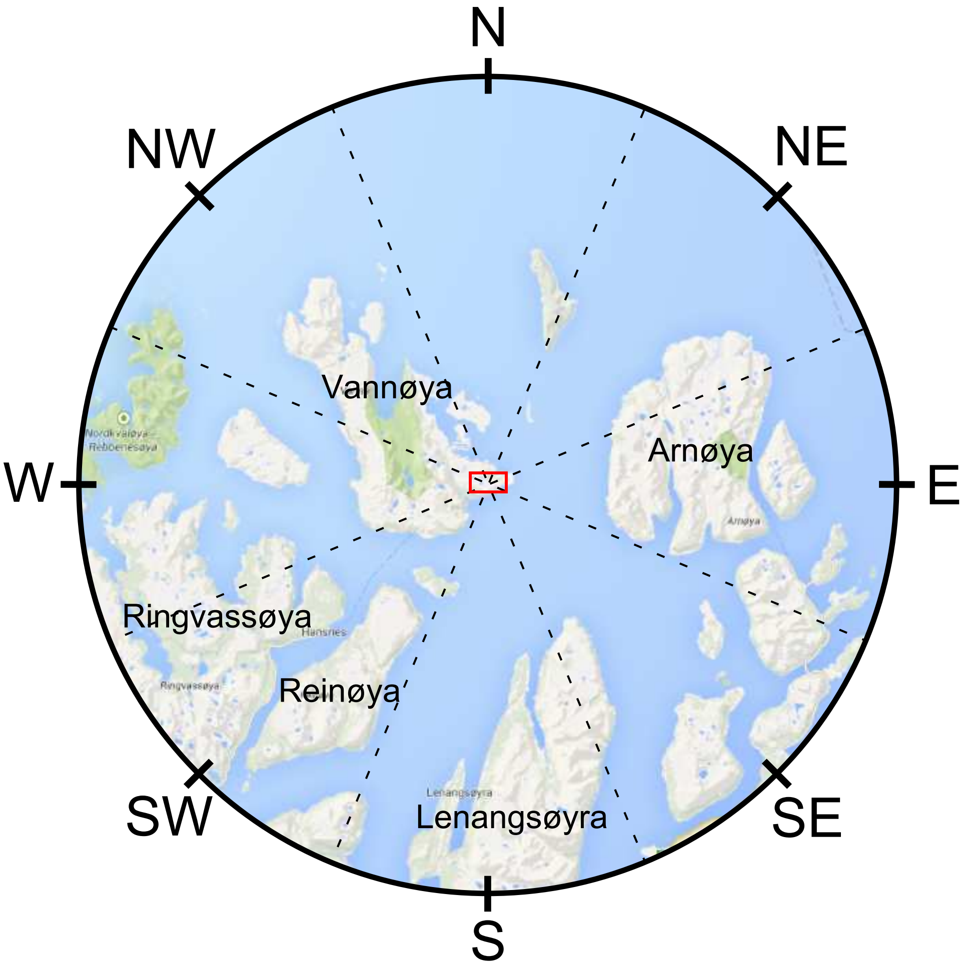

Figure 4.3: Fakken wind farm (red rectangle) with the surrounding area and directions shown.

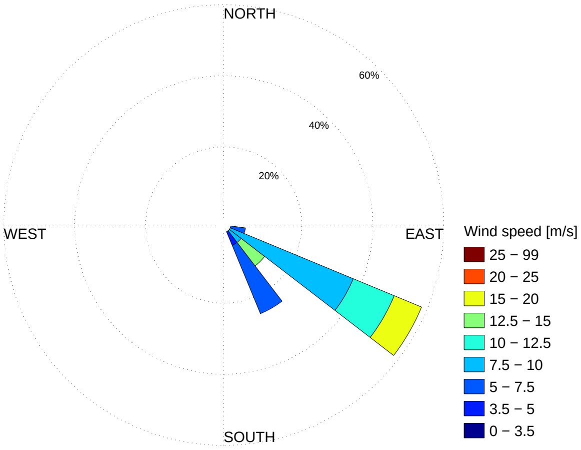

Figure 4.4: Rose diagram of in-situ measurements from the meteorology station at Fakken wind farm, 27. October 2013 (UTC-time).

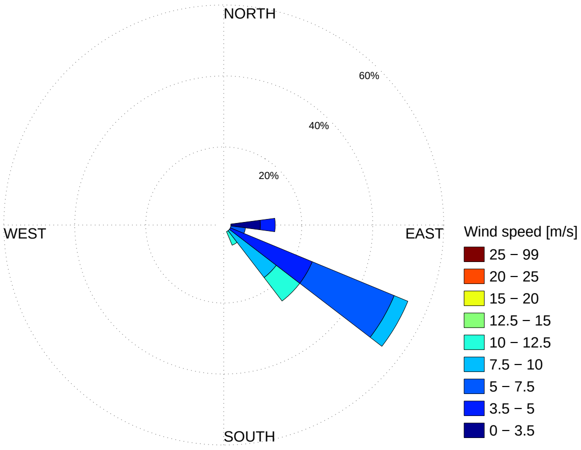

Figure 4.5: Rose diagram of the forecast wind at Fakken wind farm ,27. October 2013 (UTC-time).

In Figure 4.6 the measured values follows quite well the same trend as the theoretical power curve, with some distinguished outliers observed. The majority of measurements are seen below 1000 kW and 10 m/s.

For the power curve using forecast wind speed the same trend can be seen, but is observed to be drastically shifted towards lower wind speeds. This is especially seen by the high number of rated power observations occurring at very low wind speeds. This corresponds with the lower wind speeds that was seen in the rose diagrams between measured and forecast data. In addition a higher spread is observed over the whole specter, especially below 1000 kW and 10 m/s compared to Figure 4.6.

### 4.2.1 Case study

A case study of 27. October 2013 are shown in Figure 4.8 and Figure 4.9, using the measured and forecast wind speed respectively. In these plots it is much easier to see the difference between real and predicted data. For measured values, the data points lies close to the theoretical power curve with a relatively small spread, while for the forecast values, all the data points are located to the left side of the theoretical curve. However, the forecast data still follows the same trend. It should also be noted that for this particular day almost the entire specter of wind speed and power can be observed.

## 4.3 Power, speed and direction diagrams

This section will consider how the power output from the WTG08 wind turbine changes with respect to variations in the speed and direction of the wind. All the data discussed are converted from their original 10-minute values to hourly values by applying formulas corresponding to the statistical features used. Data are recorded for one whole year, starting at 1. May 2013 and ending on the 31. April 2014.

In the following figures, there are images with equally sized rectangles which illustrates a given direction and speed interval. Each of these boxes corresponds to a given state or event and the color represent the intensity measured. Dark red means higher intensity, while dark blue means a low intensity. If a rectangle is white, no observations of this particular event were recorded.

Be aware that the first and the three last wind speed states on the x-axis have a broader speed interval, thus a higher number of recordings from these states could be expected. The reason for splitting these states up in this order is to be able to easier analyze special features of the power production occurring at cut-in, cut-off and rated wind speeds. It should also be noted that all data corresponding to 0° directional measurements were omitted. This is because in meteorology, 0° means that there is not high enough

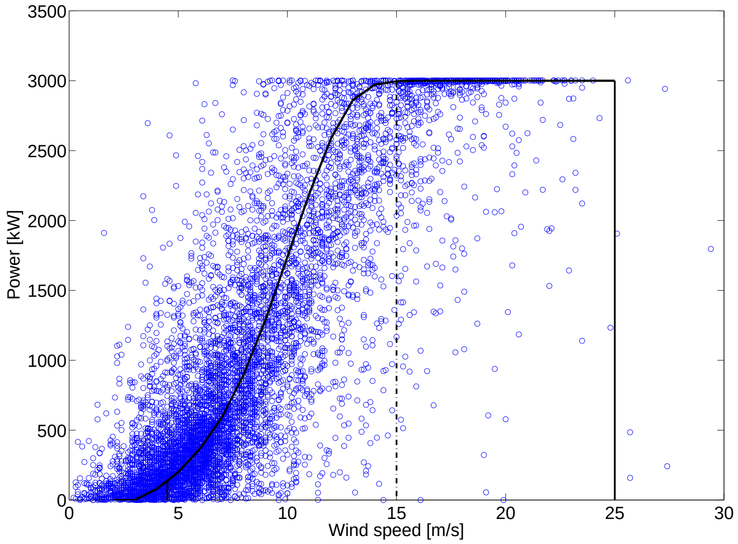

Figure 4.6: Theoretical power curve (black) with measured power output from WTG08 as a function of measured wind speed (blue circles). Time period is 2. May 2013 - 31. March 2014 (UTC-time).

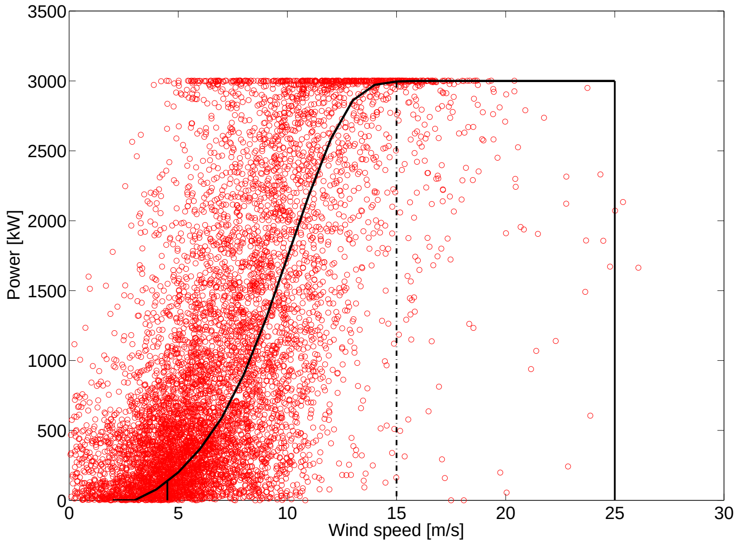

Figure 4.7: Theoretical power curve (black) with measured power output from WTG08 as a function of forecast wind speed (red circles) .Time period is 2. May 2013 - 31. March 2014 (UTC-time).

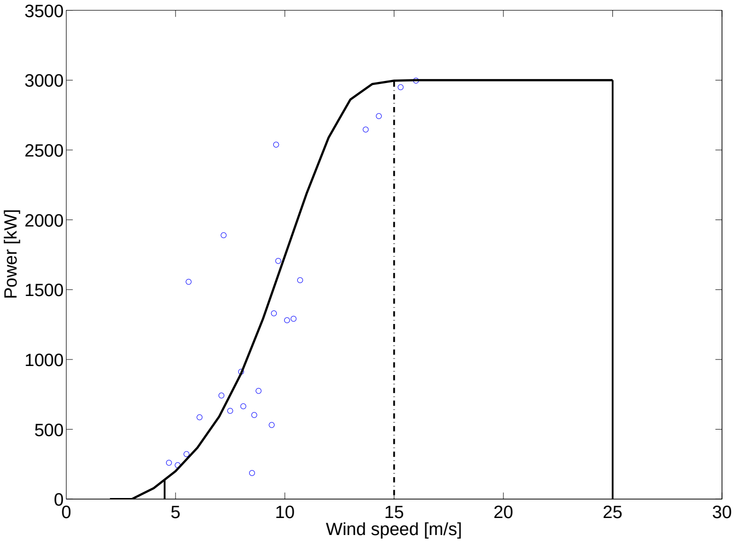

Figure 4.8: Case study of 27. Ocotber 2013 (UTC-time). Theoretical power curve (black) with measured power output from WTG08 as a function of measured wind speed (blue circles).

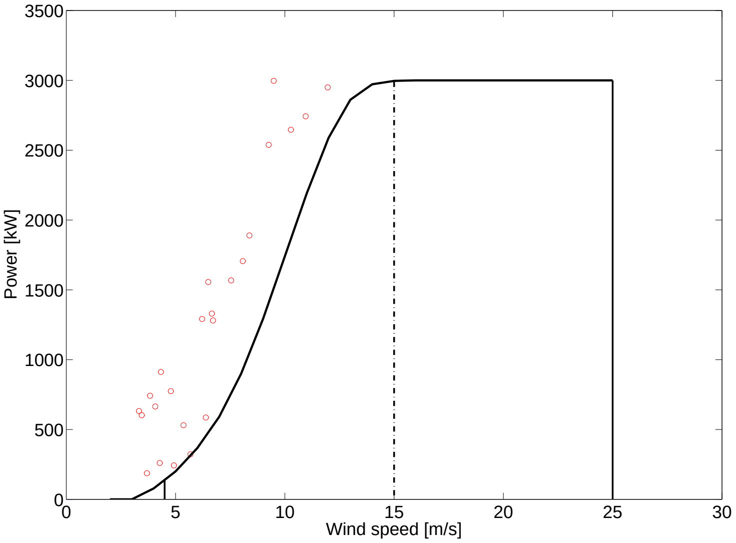

Figure 4.9: Case study of 27. Ocotber 2013 (UTC-time). Theoretical power curve (black) with measured power output from WTG08 as a function of forecast wind speed (red circles) .

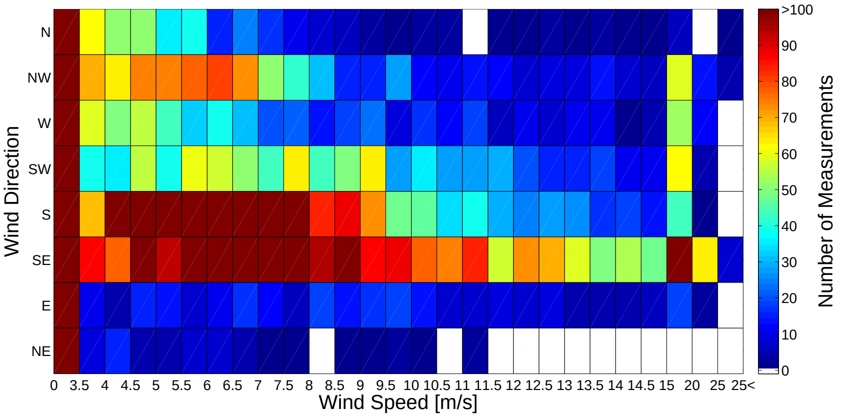

Figure 4.10: The number of measurements observed for a given wind speed and direction in the period 1. May 2013 - 31. April 2014 (UTC-time), using hourly averaged data.

wind speed for a wind direction to be measured, and should therefore not be considered in this case. When it is possible to measure a direction, 360° is used instead.

### 4.3.1 Number of observations

First consider Figure 4.10, which shows the number of observations recorded in the time period for a given wind speed (x-axis) and wind direction (y-axis) state. This is similar to the rose diagrams seen in Section 4.1, however it is for a broader time period, as the data in this section is not considering the weather forecasts, and the data points are now obtained as averages over an hour.

The distribution of the observations show some clear trends. In general low wind speeds occur in all directions with a high number of observations available. The definitely most dominant wind directions are from south and southeast followed by northwest and southwest. Winds from eastern and especially northeastern directions are not occurring frequently and high speed winds from northeast are not recorded in the time period at all. Low wind speeds are observed more frequently than high wind speeds.

### 4.3.2 Standard deviation

The standard deviation (STD) of the measured power output are shown in Figure 4.11. This is a statistical measure for how much the observations deviate from each other, i. e. how much spread there is in the recorded data. A higher value means a greater spread.

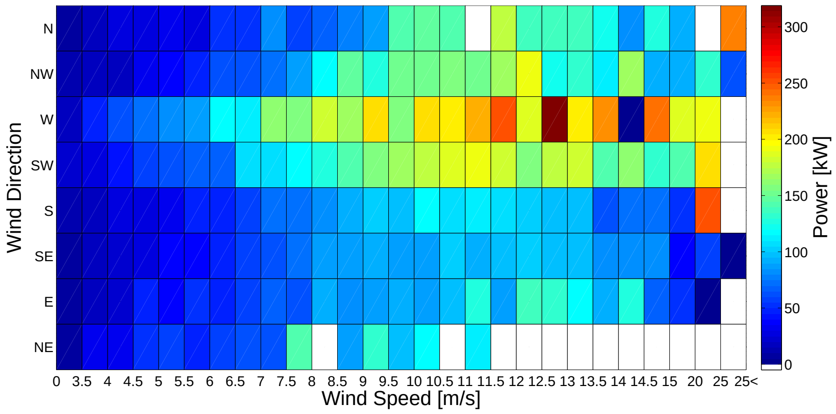

Figure 4.11: The standard deviation of the observed power output for a given wind speed and direction in the period 1. May 2013 - 31. April 2014 (UTC-time), using hourly averaged data.

The most interesting feature in this plot is the high STD seen for westerly winds and to a high degree also for winds blowing from southwest and northwest. A high variation are also observed for wind speeds in the states around 25 m/s for several of the wind directions. In general a higher STD are seen for higher wind speeds, decreasing with decreased speed. Power output for the four bottom rows, directions going from south to northeast, are more or less stable over the entire wind speed range.

### 4.3.3 Averages

Two methods for analyzing the average of the power output as a function of wind speed and wind direction are seen in Figure 4.12. In the upper subplot the arithmetic mean has been used to calculate the average, while the median is used in the lower subplot. The reason for choosing both of these averaging methods are to better illustrate the average of the power output. For normally distributed data the arithmetic mean is a good method for finding the average of the sample, however this method is very sensitive to outliers in the sample, i. e. skewed distributions. In this case the median will give a better estimate of the average. Note that in these subfigures two additional rows are added to the y-axis. One is intentionally left empty while the other shows the power curve for the WTG08 wind turbine, which can be used as a reference when analyzing the data.

As expected, the general trend is that the power output increases for an increased wind speed until the wind reaches the cut-off speed, where the power production suddenly drops. The power output in the lower wind speed specter follows the power curve quite well for all directions. At about

7 - 10 m/s some outliers are seen, which actually have a higher power output than what should be expected from the power curve.

For wind speeds above this however, more variations in the power output can be observed. Here the power output seems to generally be lower than the corresponding values seen for the power curve. The row which deviates the most from the power curve is the row corresponding to western winds. In this direction the rated power output are not seen in either the mean or the median plot for any wind speeds and the power output is relatively far below the expected output.

At the interval between 14 - 14.5 m/s for a western direction, only two observations have been recorded and both at zero values. This suggest that a special event have occurred while these measurements were recorded.

Comparing the two columns representing the rated power output, i. e. wind speeds of 15 - 25 m/s, for both the mean and median, the first column corresponds well with the power curve, while the second column have a noteworthy lower average power output. An exception is in the case of easterly and southeasterly winds, where only the mean values are lower, while the median values are at the rated power. These two cases will be studied in more detail in the following case study.

### 4.3.4 Case study

In this case study two states will be looked into for a more detailed analysis. The first is the western wind direction for the wind speed interval 15 - 20 m/s and the second state is for the southestern direction, with the same wind speed interval.

Figure 4.13 shows the distribution of the observed wind power, using the arithmetic mean for averaging.

For the upper plot, i. e. southesterly winds, the power output is observed within the range of 2900 - 3000 kW in almost 70 % of the cases, with the rest of the observations being close to the rated output. In the lower plot however, the distribution is completely different. Here 15 % of the observed winds have zero power, with rated power output recorded in less than 15 % of the total observations. Most of the wind power measurements are seen above 1750 kW, but much more evenly spread out compared to the southeastern direction.

## 4.4 Markov model

### 4.4.1 Leave one out method

A total of 18 Markov chain (MC) models with various input parameters where tested using the leave one out method (see Section 3.3.3). Additionally two persistent models (PM) were run for each month separately and for the

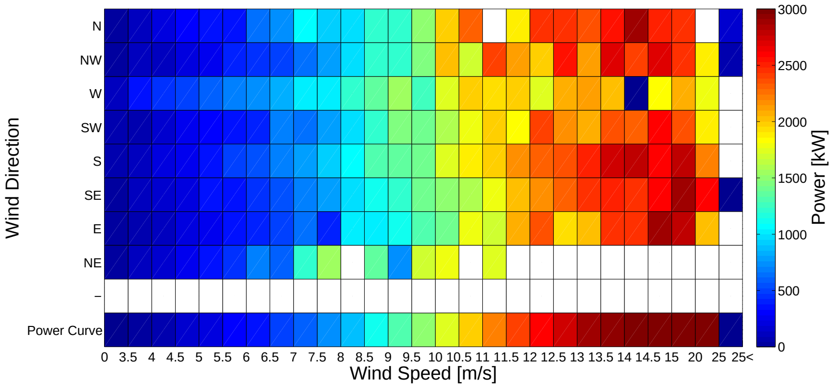

(a) Mean.

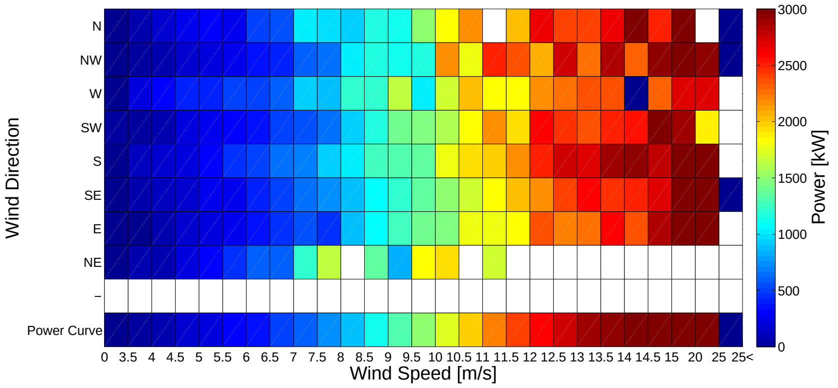

(b) Median.

Figure 4.12: The mean (a) and median (b) power output observed for a given wind speed and direction in the period 1. May 2013 - 31. April 2014 (UTC-time), using hourly averaged data. Last row displays the corresponding power curve for the WTG08 turbine.

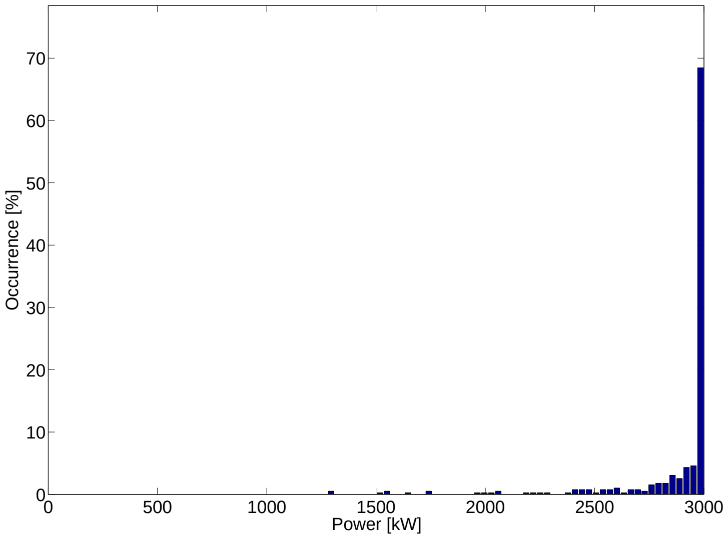

(a) Southeast

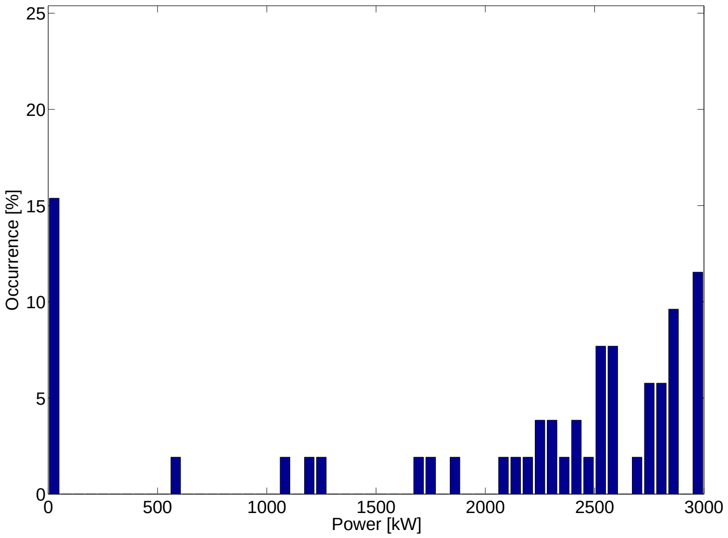

(b) West

Figure 4.13: The distribution of mean wind power observed for wind speeds in the interval between 15 - 20 m/s for winds from southeast (a) and west (b) in the period 1. May 2013 - 31. April 2014 (UTC-time), using hourly averaged data.

whole period, to be used as reference models. The first PM use $m = 1$ in Equation 3.5, i. e. a model which states that the average power output over the next hour equals the average power output over the last hour. Second PM use $m = 2$, which means that the average power output over the last hour equals the power forecast of between next hour and two hours into the future. The latter is the model currently used to forecast power production at Fakken wind farm and is therefore of special interest for comparison. By definition, no training period are required for the PM (see Section 3.3.2).

Combining each independently tested month, it was possible to obtain a dataset containing test data for the whole period. For every model, the normalized root mean square error (NRMSE) were calculated for the combined dataset and the results are seen in Table 4.1.

As expected, M1 performs better than M2, however as the power production companies must give the expected power output between $t_1$ and $t_2$ at time $t_0$, only M2 will be applicable in practice and this is the reason why the current model used for Fakken wind farm is M2. Even so, it is still interesting to use M1 as a comparison.

M3 to M11 are MC models with various input parameters, while M12 to M20 have the same input parameters, but in this case the MC models are combined with M2. These combined models use the MC as default, but if the current state used to predict $P(t_2)$ are not found in the transition matrix, i. e. no such event have been previously recorded, the model will instead use $P(t_0)$ as a forecast of $P(t_2)$, which is the M2 persistent model. The default option for MC would be to choose state 1 instead, which is a zero power output state.

Of the MC models, M4 and M7 have the lowest NRMSE over the entire time period and their equivalents M13 and M16 have the lowest NRMSE of the combined models. These models outperform the currently used M2, only by using measured and forecast wind speed to predict the future power output. The best performing model, M16, has a 2.24 % lower NRMSE value than M2 during the time period tested and has only got a 3.46 % higher NRMSE value than M1.

The worst performing models are M10 and M11, which consist of many input parameters of measured and forecast wind speed and direction, with NRMSE values of 25.70% and 27.54% respectively.

In general higher NRMSE can be observed for the MC models compared to their equivalent combined models, with exception of M4 and M13.

Figure 4.14 shows the NRMSE as a function of months for the M1, M2, M4 and M7 models. Comparing the models with each other it can be noted that M1 beat the three other models in performance for every month, as would be expected from the table values seen in Table 4.1, but with M4 and M7 being really close in July and August. The persistent models M1 and M2 are observed to have relatively equal NRMSE curves throughout the time period. In general the M4 and M7 performs better than the M2

| Type | Model # | Input Parameters | Output Parameters | NRMSE (%) |
|---|---|---|---|---|
| PM | | | | |
| | 1 | $P_{t_0}$ | $P_{t_1}$ | 13.38 |
| | 2 | $P_{t_0}$ | $P_{t_2}$ | 19.08 |
| MC | | | | |
| | 3 | $P_{t_{-1}}$, $P_{t_0}$ | $P_{t_2}$ | 23.07 |
| | 4 | $U_{t_{-1}}$, $U_{t_0}$ | $P_{t_2}$ | 17.20 |
| | 5 | $U_{t_{-1}}$, $U_{t_0}$, $P_{t_0}$ | $P_{t_2}$ | 18.75 |
| | 6 | $\hat{U}_{t_0}$, $\hat{U}_{t_2}$, $P_{t_0}$ | $P_{t_2}$ | 22.58 |
| | 7 | $U_{t_{-1}}$, $U_{t_0}$, $\hat{U}_{t_2}$ | $P_{t_2}$ | 17.58 |
| | 8 | $U_{t_{-1}}$, $D_{t_{-1}}$, $U_{t_0}$, $D_{t_0}$ | $P_{t_2}$ | 20.52 |
| | 9 | $U_{t_0}$, $D_{t_0}$, $\hat{U}_{t_2}$ ,$\hat{D}_{t_2}$ | $P_{t_2}$ | 21.02 |
| | 10 | $U_{t_{-1}}$, $U_{t_0}$, $D_{t_0}$, $\hat{U}_{t_2}$ ,$\hat{D}_{t_2}$ | $P_{t_2}$ | 25.70 |
| | 11 | $U_{t_{-1}}$,$D_{t_{-1}}$,$U_{,t_0}$, $D_{t_0}$, $\hat{U}_{t_2}$ ,$\hat{D}_{t_2}$ | $P_{t_2}$ | 27.54 |
| MC + M2 | | | | |
| | 12 | $P_{t_{-1}}$, $P_{t_0}$ | $P_{t_2}$ | 22.49 |
| | 13 | $U_{t_{-1}}$, $U_{t_0}$ | $P_{t_2}$ | 17.23 |
| | 14 | $U_{t_{-1}}$, $U_{t_0}$, $P_{t_0}$ | $P_{t_2}$ | 17.57 |
| | 15 | $\hat{U}_{t_0}$, $\hat{U}_{t_2}$, $P_{t_0}$ | $P_{t_2}$ | 20.96 |
| | 16 | $U_{t_{-1}}$, $U_{t_0}$, $\hat{U}_{t_2}$ | $P_{t_2}$ | 16.84 |
| | 17 | $U_{t_{-1}}$, $D_{t_{-1}}$, $U_{t_0}$, $D_{t_0}$ | $P_{t_2}$ | 18.16 |
| | 18 | $U_{t_0}$, $D_{t_0}$, $\hat{U}_{t_2}$ ,$\hat{D}_{t_2}$ | $P_{t_2}$ | 17.79 |
| | 19 | $U_{t_{-1}}$, $U_{t_0}$, $D_{t_0}$, $\hat{U}_{t_2}$ ,$\hat{D}_{t_2}$ | $P_{t_2}$ | 18.89 |
| | 20 | $U_{t_{-1}}$,$D_{t_{-1}}$,$U_{t_0}$, $D_{t_0}$, $\hat{U}_{t_2}$ ,$\hat{D}_{t_2}$ | $P_{t_2}$ | 19.11 |

Table 4.1: Overview of the performance of persistent models , Markov chain models and combined Markov chain and persistent models (MC + M2) for various input parameters.

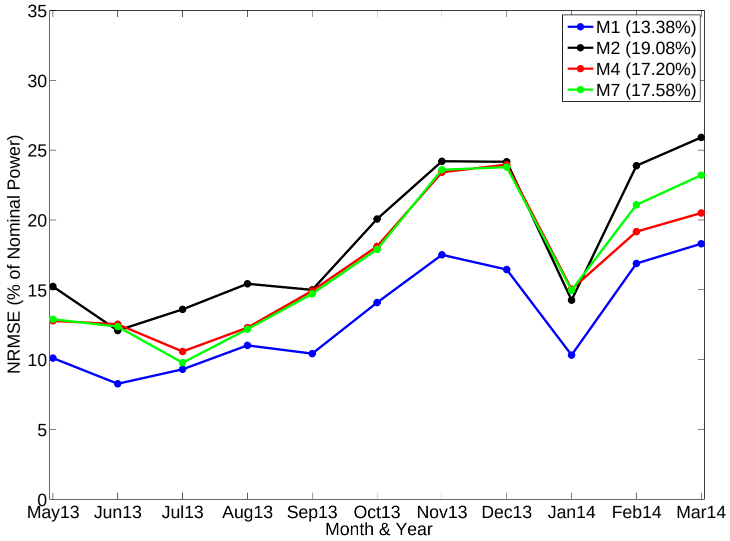

Figure 4.14: The NRMSE of M1, M2, M4 and M7 shown for each month with the NRMSE for the whole time period given in parenthesis behind the respective model legend.

model, especially in July and August 2013 and February and March 2014. From September to January M2, M4 and M7 have relatively equal NRMSE values.

Looking at how the performance changes with time, all models are seen to perform better in the late spring and summer months compared to the autumn and winter months. An exception is January, which breaks the general trend.

Corresponding curves for the combined models are seen in Figure 4.15, with M13 and M16 plotted with the reference models M1 and M2. The trends seen here are similar to those seen in Figure 4.14 with only some minor changes. M16 perform better in November and December than was the case for the equivalent M7 model and this is also the case for February and March, where M16 now are relatively equal to M13.

### 4.4.2 Case study

A case study of the power forecasts of model M2, M4 and M16 compared to the real power output for 27. October 2013 (UTC-time) are given in Figure 4.16. Model M7 and M13 were emitted in this case, as their plots were not significantly different from their equivalent models M16 and M4 for this day.

Starting with M2, it is easy to see that this curve is a 2 hour delayed version of the real power output. For small changes the M2 model forecast

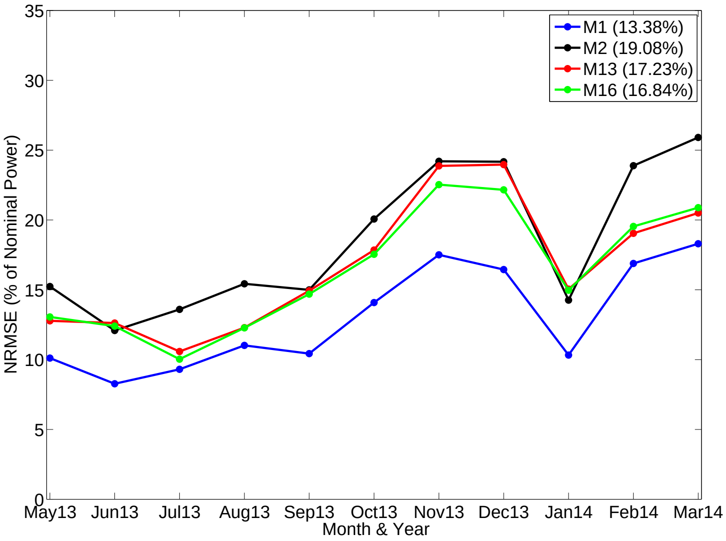

Figure 4.15: The NRMSE of M1, M2, M13 and M16 shown for each month with the NRMSE for the whole time period given in parenthesis behind the respective model legend.

relatively good the real power output, for instance seen in the time periods 01 to 05, 11 and 12 and 15 to 19. However, for greater changes and variation in power output, the M2-model deviates more from the real curve. This is seen especially when the power output changes relatively fast from rated output to low power values in only a few hours around 06 to 09. In general the M2 are observed to predict lower values than what was measured at 13 and 14 and at 20 to 24, with an exception at 22.

The M4 model dwells longer on the rated power output, compared to M2 and M16, before it suddenly decrease drastically the forecast in just a few steps. It underestimate the power output at similar times as the M2, namely at 13, 14 and 20 to 24, also with an exception at 22 where it predicts accurately the power output.. Also at 15 to 17 the M4-model overestimate.

The M16 model manage to follow the rapid decrease in power output during the nighttime and morning to a higher degree than what was seen for M2 and M4. It should also be noted that it lies at a lower power from start, compared to the other models. Like the previous models, M16 also underestimates the power output at 13 to 14, but at 15 to 17 it overestimate quite much more than the M4-model, It underestimate at 19 and 20, overestimates at 22, before going back to underestimating the power output at 23 and 24.

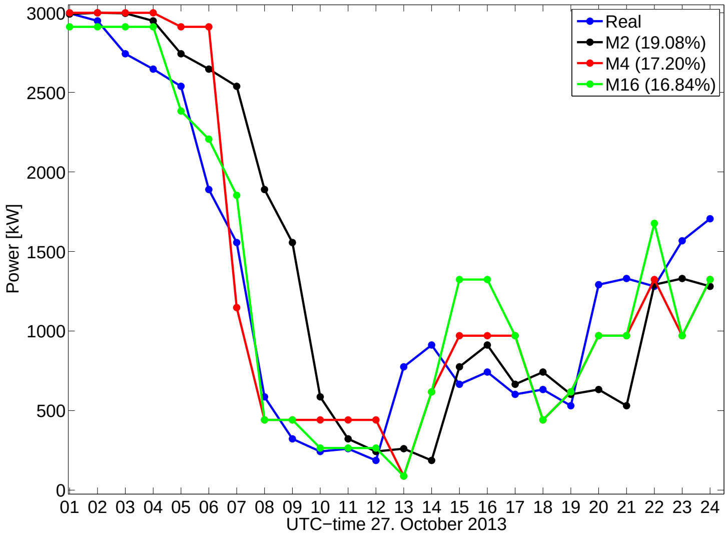

Figure 4.16: Case study of 27. October 2013 (UTC-time) showing the predicted power output from the M2 (black), M4 (red) and M16 (green) models compared to the measured power output (blue). The NRMSE corresponding to each model for the whole time period are given in parenthesis.

# Chapter 5

# Discussion

## 5.1 Wind roses

In general the results from Section 4.1 show that the wind seem to favor directions corresponding to straits between the many surrounding islands of Vannøya. A reason for this are likely due to the high mountains and mountain ranges located on the islands, making the straits less resistant pathways for the wind.

For the measured data, the rose diagram showed a good portion of the wind blowing from north-northeast. This suggests that the winds blowing in from the ocean follows the curvature of the mountain range on Vannøya, crossing the island from the north-northwest to the south.

Few winds were observed from east and west compared to the other directions. This is likely the result of Arnøya to the east working like an obstacle to any natural wind flows from this direction, and the mountain range to the west of Fakken.

The results also showed that the predicted and measured wind direction had some major differences. This could be due to the resolution of the NWP from AROME-Norway. Even though the resolution is greatly improved from previous models, a resolution of 2.5 km will still have some difficulties in accurately recreating the topography of areas with huge variations and rapid changes in height, such as mountain ranges. The topography in the model would therefore be smoothed, reducing the obstacle-effects which could be seen from mountain ranges. For instance the AROME-Norway model predicts Fakken wind farm at 20 meter above sea level, while the true height is approximately 57 meter. This could also be the reason for the shifting of direction from northeast-north to north from the measured to forecast wind direction.

## 5.2 Power curve

As expected the power curve for the measured wind speed data does not follow the theoretical power curve exactly, but the trend is still clear. Main reason for this being that the meteorological station does not measure perfectly the wind speed incident on the wind turbine. Many factors could possibly contribute to measurement errors. Take for instance the variation in the wind direction, in some cases the meteorological station will be ahead of the turbine making good measurements of the incident wind, while in other cases, the direction of the wind could cause the meteorological station to be at the lee side of the turbine, which would result in the wind already having a reduced energy. The meteorological station would then be shadowed by the WTG08 turbine, as was discussed for wake effects in Section 2.6.1. Other factors could be local turbulence, wake effects, wind turbine settings and so on.

It should also be noted that both measured and forecast data are for 80 meter height, while the rotor of the wind turbine has a diameter of 90 meter, making the turbine blades span from 35 to 125 meter heights. A power curve should therefore not be used as a direct link between wind speed and the power output, but more of a indicator of the expected power output for a given speed.

The power curve from forecast wind speed gives a very clear picture of the general underestimation of wind speeds from the NWP model, this is especially seen for all the rated wind power measurements occurring at low wind speeds. This is also seen for the case study. However, it does follow the same trend, though with a larger spread. It could therefore be possible to use a correction factor to try and reduce the effect of underestimation.

## 5.3 Power, speed and direction diagrams

Like with the rose diagrams seen in Section 4.1, Figure 4.10 also show that the wind patterns corresponds well with the observed straits between the islands surrounding Fakken seen in Figure 4.3.

The standard deviation values seen in Figure 4.11 showed some interesting results. Winds blowing from westerly direction had significantly higher STD-values compared to other directions, suggesting a higher degree of unstable winds. This could very well be related to the mountain wave phenomena discussed in Section 2.6.2, which would mean that winds passing over the mountain range to the west would be more turbulent and therefore create a higher spread in the measured power output.

Even so it should also be noted that the states with a higher number of observations does seem to have a lower STD, vice versa, comparing Figure 4.10 and Figure 4.11. A contradiction to this hypothesis is the eastern and northeastern direction where both low number of measurements and low STD-values are observed. However, as low number of observations may easily skew the STD-measure, it would be wise to look at some more data before drawing any conclusions regarding the mountain waves.

For the last two wind speed states in the STD-figure high values are observed for most of the directions. This could be expected, as these states corresponds to the cut-off speed where small changes in wind speed may lead to a sudden drop in power output due to the turbine being shut-down to avoid fatigue and for safety reasons.

In Figure 4.12 the mean and median of the power output were shown. Rated power output were not observed at all for winds from the west in any of the subfigures, and neither from northwest or southwest in the mean subfigure. This means that there is definitely some incidents occurring for westerly winds. Also in this case the observation fits very well with the mountain wave phenomena, as more turbulent winds would lead to difficulties in obtaining efficient power production and generally give a lower power output, as seen here.

Variations between the mean and median values was especially seen for wind speeds from 15 - 25 m/s. These variations can be divided into two cases. The first case is when the median shows a rated power output, while the mean shows a lower power output. In this case there are a few outliers in the data sample which pulls down the mean estimate, while the majority of the measurements are observed with the rated power output. This will cause the mean to be reduced, while the median will still show the rated power output. In the second case, reduction in both the mean and median values are observed. For this to happen, the majority of the observations must have a lower power output than the rated power, as only this may cause the median to drop.

This corresponds very well with what was seen in Figure 4.13. These distributions clearly show that for southeastern wind directions the power output are much more consistent, with the majority of values being close to the rated power. The few outliers will naturally pull down the mean value, while the median will indicate rated output. For western winds however, the distribution is much more spread with many occurrences of what could be cut-off wind speeds.

The case study also clearly shows the occurrence of turbulent winds from a western direction and how this affects the power production.

## 5.4 Markov chain models

In general the MC models have higher observed NRMSE values than the combined MC and M2 models. This indicates that there are occurrences where the currently observed state have not been recorded before, leading to the MC model prediction zero power output, while MC + M2 model use the current power output. Generally lower NRMSE for the combined models suggest that the current power output is typically closer to the real power output in 2 hours than the zero power output state. Exception are the M4 and M13 models. In this case the guess of zero power output is most likely closer to the real power than the current power production.

Another trend seen in the Table 4.1 are how the NRMSE depends on the number of input parameters, which is equivalent to the size of transition matrix. M10 and M11 have the highest NRMSE and also the highest number of input parameters and combined states. As discussed in Section 3.3.3 this probably cause the model to be over-trained. In general too many input parameters and number of states for these parameters would increase the complexity of the model, making it less capable of predicting new values, while too few input parameters or too few states for these would lead to under-training of the model and also poor performance.

Take for instance M11, with three wind speed and three wind direction input parameters. Combined with the power output parameter, these would make a 373248X20 transition matrix, with 7 464 960 possible states! Of course in practice, all these states would not be real possible events, making some of them redundant. However, it would require vast amounts of data the fill all the probable states. Even for a small transition matrix, such is the case for M4, it would be hard to fill all the elements of the matrix with observations using only measurements from 11 months. See for instance Figure 4.10 where no high speed winds from northeast have been observed, even though they are possible states in the transition matrix. From this it is possible to conclude that a Markov chain model would be more accurate for a higher number of observations used to fill the transition matrix.

In Figure 4.14 and Figure 4.15 the M2 model is observed to follow the same trends as the M1 mode. Reasons for this is probably due to both using the same predictor, namely the persistent model.

An interesting observation is seen between the M7 and M16 models in the two figures. For November, December, February and March, the M16 perform much much better than the M7, indicating that in these months a lot of observation which has not been recorded before in the transition matrix are seen. Looking at the NRMSE curves from a seasonal perspective, it seems to be generally lower prediction errors for months characterized by more calm and stable weather, such as late spring and summer months, while more errors are made when the autumn and winter weather steps in, usually consisting of much more unstable weather. January 2014 was observed as a extraordinary dry and calm month, with almost no precipitation, which may be the reason why all models made relatively good wind power predictions for this month. This seasonal trends may also be the cause of the M16 performing better than M7, as unstable weather could very well indicate weather conditions which have not previously been recorded.

# Chapter 6

# Conclusions

A statistical analysis was conducted for Fakken wind farm based on measurements recorded in the time period 1. May 2013 - 31. April 2014 and NWP data in the time period 2. May 2013 - 31. March 2014. This showed that the main wind directions are from the straits between Arnøya and Lenangsøyra to the southeast and between Rainøya and Lenangsøyra to the south. Winds blowing in from the ocean to the north and northeast are observed to follow the mountain range on Vannøya, leading to north-northwesterly winds at Fakken wind farm. Few winds were observed from the west and east. This indicates that Arnøya to the east and the mountain range on Vannøya, west of Fakken, are working as obstacles for the wind flows from these directions. Only a few observations were made of winds from northeast, mainly being low speed winds below 10 m/s.

Wind forecast showed similar trends, but the wind speed were generally underestimated and the wind directions were more evenly distributed and skewed. This can be concluded as being a result of how the AROME-Norway NWP model the topography, reducing the affects from the surrounding mountains.

High standard deviation of the power output from the WTG08 reference turbine was observed for winds mainly from west, but also from northwest and northeast. In addition low mean and median values were observed for westerly winds, indicating that winds from the west are more turbulent than any other direction. This is most likely the result of mountain waves occurring for winds crossing over the mountain range on Vannøya, significantly influencing the power production.

A total of 18 power prediction models were developed, of which 9 were based on Markov chains and the remaining 9 were combined models based on Markov chains and a persistent model. The performance were evaluated using the normalized root mean square error and compared with two persistent models.

The currently used power prediction model at Fakken wind farm, a persistent model with a prediction horizon of $m = 2$, was found to have a NRMSE of 19.08%. Several of the models developed in this study were found to have lower NRMSE than the currently used model, of which the best performing model had a NRMSE of 16.84 %. This model use as input the currently measured wind speed and in the previous hour, together with forecast wind speed in 2-hours. This 2.5% lower NRMSE corresponds to approximately $3.1 \cdot 10^6$ kWh of the anually electricity production from Fakken wind farm.

These discoveries indicates a great potential in using power prediction models based on Markov chains going directly from various input parameters, such as measured and forecast wind speeds, to predicted power output.

## 6.1 Further research

There are several features which could improve the performance of the wind power prediction models discussed in this study.

Currently the states are more or less linearly spaced for each parameter and does not take into consideration how the available observations are distributed. It could therefore be beneficial to look into various clustering methods and how they could be used to create more ideal states.

A high number of input parameters and/or a high number of state intervals results in a high number of empty states with no observations recorded. This will cause problems when evaluating new data, as these might not have been previously observed, leading to the MC models choosing a 0 kW wind power forecast by default. It is suggested to replace this default behavior with a method for finding the nearest neighbor in the transition matrix instead.

It would also be very interesting to combine the MC models with the work of Yoder et al. [2013], using the suggested model of 1 hour ahead categorical change in wind power as an indicator for the MC models.

Only one of the four daily weather forecast issued by AROME-Norway have been used in this study. The first hours of every forecast are usually characterized by a higher degree of noise. Combining forecasts issued at different times, would make it possible to avoid this noise and obtain more accurate wind forecast.

# Bibliography

John Andrews and Nick Jelley. *Energy Science, principles, technologies, and impacts.* Oxford University Press, 2007.

Trygve Aspelien and Morten Køltzow. AROME-Norway From experiments to official public forecasts for the whole wide world. [Online], April 2013. URL `http://www.cnrm.meteo.fr/aladin/IMG/pdf/ASM_AROME-Norway201304_TA.pdf`. Accessed on May 16th 2014 at 10:12.

Holger Babinsky. How do wings work? *Physics Education*, 38(6):497–503, 2003.

Heiko Balzter. Markov chain models for vegetation dynamics. *Ecological Modelling*, 126(2):139–154, 2000.

Arthur Bossavy, Robin Girard, and George Kariniotakis. Forecasting ramps of wind power production with numerical weather prediction ensembles. *Wind Energy*, 16(1):51–63, 2013.

Godfrey Boyle. *Renewable Energy.* Oxford University Press, 2004.

BP. BP statistical review of world energy june 2013, 2013.

A. Carpinone, R. Langella, A. Testa, and M. Giorgio. Very short-term probabilistic wind power forecasting based on Markov chain models. pages 107–112, 2010.

K. Conradsen, L. B. Nielsen, and L. P. Prahm. Review of Weibull statistics for estimation of wind speed distributions. *Journal of Climate and Applied Meteorology*, 23(8):1173–1183, 1984.

Philippe Drobinski and Corentin Coulais. Is the weibull distribution really suited for wind statistics modeling and wind power evaluation? *arXiv preprint arXiv:1211.3853*, 2012.

Stefan Emeis. *Wind Energy Meteorology Atmospheric Physics for Wind Power Generation.* Springer-Verlag Berlin Heidelberg, 2013.

EREC. Renewable energy the solution to climate change, 2005.

Douglas C. Giancoli. *Physics principles with applications.* Pearson Education International, sixth edition, 2005.

Gregor Giebel, Richard Brownsword, George Kariniotakis, Michael Denhard, and Caroline Draxl. The state-of-the-art in short-term prediction of wind power: A literature overview. Technical report, ANEMOS. plus, 2011.

F. González-Longatt, P. Wall, and V. Terzija. Wake effect in wind farm performance: Steady-state and dynamic behavior. *Renewable Energy*, 39 (1):329–338, 2012.

Zack Guido. Climate dynamics. [Online], September 2008. URL `http://www.southwestclimatechange.org/climate/global/dynamics`. Accessed on 11.05.2014 at 15:05.

Robert V. Hogg and Allen T. Craig. *Introduction to Mathematical Statistics.* Macmillan Publishin CO.,Inc., fourth edition edition, 1978.

James R. Holton and Gregory J. Hakim. *An introduction to dynamic meteorology.* Academic press, 2012.

John Houghton. *Global Warming the complete briefing.* Cambridge University Press, fourth edition edition, 2009.

IPCC. Summary for policymakers. in: Climate change 2014: Impacts, adaption, and vulnerability. Contribution of Working Group II to the Fifth Assessment Report of the Intergovermental Panel on Climate Change, 2014.

Morten Jacobsen. Statistical analysis of wind velocities at Fakken wind farm on Vannøya in Troms., 2013. Project paper, UiT The Arctic University of Tromsø.

S. Rao Jammalamadaka and Ambar Sengupta. *Topics in circular statistics*, volume 5. World Scientific, 2001.

C. G. Justus, W. R. Hargraves, and Ali Yalcin. Nationwide assessment of potential output from wind-powered generators. *Journal of Applied Meteorology*, 15(7):673–678, 1976.

F. Koch, M. Gresch, F. Shewarega, I. Erlich, and U. Bachmann. Consideration of wind farm wake effect in power system dynamic simulation. In *Power Tech, 2005 IEEE Russia*, pages 1–7. IEEE, 2005.

Alberto Leon-Garcia. *Probability and Random Processes for Electrical Engineering.* Addison-Wesley Publishin Company, Inc, second edition edition, 1994.

Henrik Madsen, Pierre Pinson, George Kariniotakis, Henrik Aa Nielsen, and Torben S. Nielsen. Standardizing the performance evaluation of short-term wind power prediction models. *Wind Engineering*, 29(6):475–489, 2005.

Robert P. Mahan. Circular statistical methods: Applications on spatial and temporal performance anaylsis. Technical report, United States Army Research Institute for the Behavioral and Social Sciances, April 1991.

Knati V. Mardia and Peter E. Jupp. *Directional Statistics*. John Wiley & Sons Limited, 2000.

Andrei Andreyevich Markov. Extension of the limit theorems of probability theory of a sum of variables connected in a chain. *The Notes of the imperial Academy of Sciences of St. Petersburg, VIII Series, Physio-Mathematical College XXII*, (9), 1907.

Melinda Marquis, Jim Wilczak, Mark Ahlstrom, Justin Sharp, Andrew Stern, J. Charles Smith, and Stan Calvert. Forecasting the wind to reach significant penetration levels of wind energy. *Bulletin of the American Meteorological Society*, 92(9), 2011.

Sathyajith Mathew. *Wind Energy Fundamentals, Resource Analysis and Economics*. Springer-Verlag Berlin Heidelberg, 2006.

Dr. Brad Muller. Mountain and lee waves in satellite imagery. [Online], May 2014. URL `http://wx.db.erau.edu/faculty/mullerb/Wx365/Mountain_waves/mountain_waves.html`. Accessed on 15.05.2014 at 18:46.

Norwegian Meteorological Institute. Nettet snøer seg sammen. [Online], February 2008. URL `http://met.no/?module=Articles;action=Article.publicShow;ID=727`. Acessed on May 16th 2014 at 10:33.

Norwegian Meteorological Institute. Nå blir værvarslene enda bedre. [Online], October 2013. URL `http://met.no/N%C3%A5+blir+v%C3%A6rvarslene+enda+bedre.b7C_xdfY4e.ips`. Accessed on May 16th 2014 at 10:17.

Ca A. Paulson. The mathematical representation of wind speed and temperature profiles in the unstable atmospheric surface layer. *Journal of Applied Meteorology*, 9(6):857–861, 1970.

S. A. Pourmousavi Kani and M. M. Ardehali. Very short-term wind speed prediction: A new artificial neural network–Markov chain model. *Energy Conversion and Management*, 52(1):738–745, 2011.

Hans-Holger Rogner, Roberto F. Aguilera, Cristina L. Archer, Ruggero Bertani, S.C. Bhattacharya, Maurice B. Dusseault, Luc Gagnon, Helmut Haber, Monique Hoogwijk, Arthur Johnson, Mathis L. Rogner, Horst Wagner, Vladimir Yakushev, Doug J. Arent, Ian Bryden, Fridolin Krausmann, Peter Odell, Christoph Schillings, and Ali Shafiei. Energy resources and potentials.

Sheldon M. Ross. *Introduction to Probability Models*. Elsevier Inc., 10th edition, 2010.

Peter J. Schubel and Richard J. Crossley. Wind turbine blade design. *Energies*, 5:3425–3449, 2012.

J. V. Seguro and T. W. Lambert. Modern estimation of the parameters of the weibull wind speed distribution for wind energy analysis. *Journal of Wind Engineering and Industrial Aerodynamics*, 85(1):75–84, 2000.

Y. Seity, P. Brousseau, S. Malardel, G. Hello, P. Béénard, F. Bouttier, C. Lac, and V. Masson. The arome-france convective-scale operational model. *Monthly Weather Review*, 139(3), 2011.

A. Shamshad, M. A. Bawadi, W. M. A. Wan Hussin, T. A. Majid, and S. A. M. Sanusi. First and second order markov chain models for synthetic generation of wind speed time series. *Energy*, 30(5):693–708, 2005.

SSB. Minifacts about norway 2013. [Online], May 5th 2014. URL `http://www.ssb.no/a/english/minifakta/en/main_11.html`. Acessed on May 16th 2014 at 10:35.

Henry Stark and John W. Woods. *Probability, Statistics and Random Processes for Engineers*. Pearson Education Limited, fourth edition edition, 2012.

Troms Kraft AS. Fakken vindpark. [online], July 2012. URL `http://www.tromskraft.no/om/prosjekter/fakken`. Acessed on June 2nd 2014 at 14:52.

Vaisala Oyj. *USER'S GUIDE Anemometer WAA151*. P.O Box 26, FIN-00421 Helsinki Finland, 2002a. URL `http://www.vaisala.com`.

Vaisala Oyj. *USER'S GUIDE Wind Vane WAV151*. P.O Box 26, FIN-00421 Helsinki Finland, 2002b. URL `http://www.vaisala.com`.

Vestas Wind Systems A/S. *VestasMetPanel 3000 Meteorological Station General Specification*. Alsvej 21 8900 Randers Denmark, April 2008. URL `http://www.vestas.com`.

Vestas Wind Systems A/S. *V90 3.0MW*. Hedeager 44, 8200 Aarhus N, Danmark, 2013. URL `http:\www.vestas.com`.

Ronald E. Walpole, Raymond H. Myers, Sharon L. Myers, and Keying Ye. *PROBABILITY & STATISTISCS for ENGINEERS & SCIENTISTS*. Pearson Educational International, eight edition edition, 2007.

Xiaochen Wang, Peng Guo, and Xiaobin Huang. A review of wind power forecasting models. *Energy procedia*, 12:770–778, 2011.

Megan Yoder, Amanda S. Hering, William C. Navidi, and Kristin Larson. Short-term forecasting of categorical changes in wind power with markov chain models. *Wind Energy*, 2013.